Response of square honeycomb core sandwich panels to granular matter impact

Anne Kyner , Kumar Dharmasena , Keith Williams , Vikram Deshpande , Haydn Wadley

PII: S0734-743X(17)30905-3
DOI: 10.1016/j.ijimpeng.2018.02.009
Reference: IE 3073

To appear in: *International Journal of Impact Engineering*

Received date: 23 October 2017
Revised date: 24 January 2018
Accepted date: 23 February 2018

Please cite this article as: Anne Kyner , Kumar Dharmasena , Keith Williams , Vikram Deshpande , Haydn Wadley , Response of square honeycomb core sandwich panels to granular matter impact, *International Journal of Impact Engineering* (2018), doi: 10.1016/j.ijimpeng.2018.02.009

Highlights

- The out of plane displacement of edge restrained, grade 304 stainless steel sandwich panels has been measured after impact by rapidly expanding spherical shells of water saturated granular media at various velocities.
- The radial expansion of the spherical shells was imaged using high-speed video techniques and the radial velocity shown to vary from 500 to1200 m/s. The impact pressure and transmitted impulse were also measured using a Kolsky bar positioned at a symmetric location to the panel center.
- Discrete particle-based simulations successfully predicted particle front positions, velocities, impact pressures and plate deformations.
- The study has confirmed recent predictions that the panels out of plane displacement would be less than that of an equivalent solid plate provided the deflection did not exceed the panel thickness.

Response of square honeycomb core sandwich panels to granular matter impact

Anne Kyner, Kumar Dharmasena, Keith Williams*, Vikram Deshpande** and Haydn Wadley

Department of Materials Science and Engineering, University of Virginia, Charlottesville, VA 22903, USA

*Newtec Services, Edgefield, SC, USA

** Engineering Department, Cambridge University, UK

Abstract

The deformation of square honeycomb core, stainless steel sandwich panels by the impact of explosively accelerated granular matter has been investigated and compared to results from a previous study using equivalent (same material and mass per unit area) solid plates subjected to similar impulsive loadings. Spherical explosive charges surrounded by 25-150 kg mass annular shells of water-saturated granular media (either fused silica or zirconia particles) were suspended above the center of the edge clamped test panels. The radially expanding granular particle front velocities were measured from high-speed video images, and revealed that the granular matter had been accelerated to velocities of 500-1200 m/s after detonation. A Kolsky bar was used to measure the time-dependent pressure and impulse at a position equivalent to the panel center, while the permanent deflections of the sandwich panels were determined by profilometry after the experiments. Even though fracture of electron beam welds used to attach the back face sheet to the sandwich panel core occurred in all the tests, the permanent deflections of the sandwich panel back faces were significantly less than those of equivalent solid plates, and were accompanied by minimal core compression. Discrete particle simulations of the granular matter acceleration and impact loading of the sandwich panels indicated that their superior deflection benefit arose from their high bending resistance rather than particle-structure interactions. This benefit was offset when the rear face of the sandwich was kept the same distance from the impulsive source as that of the solid plate since the impact face of the sandwich panel was closer to the impulsive source, subjecting it to a higher impulse than the solid plate. However, a substantial deflection reduction was still achieved by use of a strong core sandwich design.

Key words: impulsive loading, discrete particle simulations, sandwich panel, granular media

Communicating Author: Anne Kyner

1 Introduction

The deformation of structures resulting from nearby explosions has been a topic of considerable research interest for many years [1-6]. The problem's complexity arises from the difficulty of precisely predicting or measuring the impulsive loads applied to a structure by an explosive event, and the theoretical challenges associated with calculating the structure's resulting time dependent deformation and fracture. For example, the same explosive event applies quite different time dependent loads when it occurs underwater, in air, or is covered (buried) by soil. This arises from differences in the mechanisms by which momentum is transferred from the detonation event to the medium by which it is propagated towards a structure, and by subsequent interactions with the impulse-transporting medium and the structure's dynamic motion during momentum transfer.

Fundamental work by Taylor [7] and by Cole [8] investigated the effects of the dynamic motion of a structure as an underwater propagated shock front impacted a free plate. They showed that if the plate had sufficiently low inertia, it could be displaced during the shock front interaction, and both the reflected impulse and that applied to the structure were reduced. Numerous studies subsequently sought to exploit this fluid structure interaction (FSI) effect through use of sandwich panels with light impact-side face sheets and compressible (but stretch resistant) cores [9-13]. The objective was to permit out-of-plane deflection of the impact face during shock loading while reducing macroscopic bending of the sandwich panel due to its high flexural rigidity and resistance to stretching [9-11]. Significant benefits were identified for some sandwich panel designs subjected to model underwater explosive events [9, 14-19].

The studies of Taylor and Cole were recently extended to air blast loading by Kambouchev et al. [20] and by Hutchinson [21]. Their work addressed the non-linear effects activated by strong air shocks, and indicated that an analogous reduction in the shock reflection coefficient, and therefore momentum transfer to a structure, could be achieved by the use of very light structures. However, the practical implementation of this result was more difficult to exploit because it required the use of very thin/low density structures during exposure to strong shock overpressures, making it likely that such structures would rupture during shock loading [12, 22]. Even though the FSI benefit for air shock loading is smaller than in water [12, 16, 20, 23],

sandwich panel structures have been designed that sustained smaller deflections than equivalent (mass and material) monolithic plates during exposure to high intensity air shocks [13]. However, this was primarily a consequence of the higher bending resistance of a well-designed sandwich panel rather than an FSI effect [12, 13]. To exploit the sandwich panel benefit, tests must usually be restricted to regions of loading where the out-of-plane panel deflections are less than the core thickness of the sandwich panel, favoring the use of strong core topologies such as the square honeycomb [13]. For larger deflections, the structural response of the panels becomes stretching dominated, and the sandwich panel benefit over the monolithic plate diminishes or even reverses for some core topologies (such as the pyramidal lattice) [9, 13]. Ideal core designs for underwater and air shock mitigation are therefore different, since the former is optimized by provision of sufficient core crushing to enable impulse reduction by the FSI effect, while the latter requires a strong core that maintains the face sheet separation necessary to maintain bending resistance [9, 13, 16].

When an explosion occurs within a granular medium such as soil, the majority of the momentum of the explosive detonation products is transferred to the soil particles which can then attain a high velocity if their mass per unit area is low (by shallow burial) [24, 25]. The momentum that is transferred to a nearby structure by these particles is governed by momentum conservation, and it therefore depends upon the incident and reflected particle velocities. Liu et al. [26] used a particle based simulation method to investigate the normal impact of sand slugs against (solid) monolithic plates, Figure 1(a). They found that particle impacts normal to a flat surface were very weakly reflected, and the transferred impulse was approximately (within 2%) that of the incident granular matter. Their study showed that the out-of-plane deflection of a normally impacted, edge clamped monolithic plate was an approximately linear function of the applied impulse.

Even though no significant FSI effect existed, the study found that equivalent sandwich panel designs (of equal mass per unit area to the monolithic plates), Figure 1(b), outperformed their monolithic counterparts, and the benefit increased when a high normalized strength core was utilized, Figure 1(c). In Figure 1(c), the normalized core strength was given by,

$$\bar{\sigma_c} = \frac{\sigma_c}{\bar{\rho_c}\sigma_Y}. \qquad (1)$$

where σ_c is the core compressive strength, σ_Y is the yield strength of the solid from which the core was made, and $\overline{\rho_c}$ is the relative density of the cellular core. Additional reductions in panel deflection were observed for sandwich panels with low aspect ratio (thick core and small span between loading points) and higher flexural stiffness. Since the small FSI effect did not result in significant variations in transferred impulses [26-28], the primary benefit of a sandwich panel subjected to impact by granular media resulted from the panel's high bending resistance [16, 26-28].

Subsequent experimental and particle-based simulation studies of explosively accelerated sand particle impact with high aspect ratio, weak (corrugated) core aluminum sandwich structures have shown that rapid dynamic deflections of low strength sandwich panel systems can induce very strong particle reflections that locally amplify the impulse applied to the structure [29]. For example, since the webs of a corrugated core are compressed slowly, compared to the rate at which the face sheet suspended between them suffers out of plane displacement, sand particles can be strongly reflected out of the plane of the overall panel from the local concavities. The resulting local amplification of impulse then leads to an instability resulting in local rupture of the face sheet near hard points. This study also showed that panel deformation and impulse amplification also occurred near lower strength (and ductility) welds. Very strong impulse amplification can also occur when reflected sand particles travelling parallel to the impacted surface are reflected out of the panel plane by picture frame-type grips that extended above the plate surface. This out-of-plane reflection induces a reaction momentum that promotes shear-off failure at the attachments [29].

This prior work identified several design principles for sandwich structures intended for high intensity granular impact mitigation. Firstly, they should utilize a strong, stretch resistant core in combination with a sufficiently thick impact face sheet that large dynamic displacements between core nodes are avoided. Square honeycomb cellular cores are ideal candidates for the core since they have both a high compressive strength and excellent in-plane stretching resistance [11, 13, 16, 30-33]. Second, the use of welds on the impact side faces should be avoided. Third, panels should provide a flat, smooth surface for uninterrupted flow of reflected particles across the structures impact surface. Finally, Figure 1 shows that the fabrication of panels from materials with a high value of $m_b\sqrt{\sigma_Y/\rho_m}$ (where m_b is the panel mass per unit

area, σ_Y is the material yield strength and ρ_m its density) is preferred, provided a higher value of yield strength does increase the susceptibility to rupture.

The objective of the study described here is to determine if a strong core sandwich panel concept can reduce the structural deflection following impact by high velocity granular matter. The recently reported [34] out-of-plane displacements of large area, 2.54 cm thick square 304 stainless steel monolithic (solid) plates impacted by radially expanding fused silica or zirconia particle shells accelerated to velocities of 500-1,200 m/s are used for a solid plate reference response. In these reference tests, a Kolsky bar was used to measure the pressure and impulse at an equivalent location to the center of the plates during five experiments of increasing incident impulse. The permanent plastic displacement of the solid plates was measured as a function of the maximum impulse and shown to scale linearly with impulse consistent with the recent analysis of Liu et al. [26]. The study presented here investigates the permanent deformation and dynamic displacements of equivalent (same mass per unit area), square honeycomb core sandwich panels made of the same 304 stainless steel alloy used for the reference study, after they were subjected to similar high intensity granular impact [34]. In the current study, the displacements and Kolsky bar pressure and impulse waveforms for the five experiments are simulated using the IMPETUS Afea discrete particle simulation code. This simulation approach was then used to analyze the plate's dynamic response. The experimental and simulation results confirm a significant reduction of the panel deflection when the mass of a solid plate is redistributed as a strong core sandwich panel. However, this benefit is reduced if the rear face of the sandwich is kept the same distance from the impulsive source as that of the solid plate. In this case, the greater panel thickness places the impact face closer to the impulsive source, subjecting it to a higher impulse than the solid plate.

2 Experimental setup

The experimental tests were conducted at the same outdoor blast testing facility (NEWTEC Services Group Inc., Edgefield, SC) used to evaluate the solid plate reference responses [34]. The 5.08 cm thick square honeycomb core sandwich panels were edge clamped to the same test platform as the (2.54 cm thick) solid plates. A schematic illustration of the overall test arrangement is shown in Figure 2. The test platform consisted of a steel picture frame to support

the target panels, a suspended spherical test charge consisting of a spherical explosive core and annular shell of water-saturated fused silica or (higher density) zirconia particles, and a strain gauge instrumented Kolsky bar to measure the applied pressure and impulse during granular particle impacts. A brief description of the test platform, charge configuration, and Kolsky bar system is given below. Full technical details can be found in Kyner et al. [25, 34].

Figure 3 schematically illustrates the test configuration geometry for the two types of targets. It shows the concentric spherical charge suspended above the center of the test targets. The charge consisted of an internal sphere of radius R_1 packed with composition C-4 explosive, surrounded by an outer sphere of radius R_2 filled with water-saturated fused silica or zirconia particles. The applied impulse was varied by changing R_1 and R_2 and the type (density) of the granular matter. Since the impulse applied to a test structure also varies with standoff distance, we attempted to use a standardized distance. The tests could have been conducted with a fixed target front (impacted) face to charge center distance or with a fixed distance from the charge center to the target back face. For the latter, the front face of the thicker sandwich structure would be closer to the charge center, and therefore suffer a higher impulse. Since this is a more conservative test of the sandwich panel benefit, an intended constant standoff distance, H_b = 47.54 cm, from the center of the test charges to the back face of both target types was attempted, as shown in Figure 3. As a result, the intended distance from the center of the test charge to the front face of the sandwich panel would be H_p = 42.46 cm while that to the front face of the solid plate would have been 45 cm. In practice, small variations in the actual standoff distances from the intended values occurred as described below.

2.1 Test platform

The test platform was identical to that used for the testing of the five reference solid plates [34]. Figure 2 shows a schematic illustration of the full test setup. A honeycomb sandwich panel is shown in Figure 3 positioned on the picture frame support base with the spherical test charge suspended above. Two high-speed cameras (Vision Research Inc., Phantom V7.3) captured the granular (sand) front position for each test shot as they radially expanded towards the Kolsky bar and test panel after detonation. The front 1.32 m length of the test panels and a 10 cm length for Shots 1 and 2 (15 cm for Shots 3-5) at the front of the Kolsky bar were spray-painted prior to testing to provide reference lengths for interpreting the high-speed video images.

2.2 Honeycomb panel design and fabrication

Square honeycomb core sandwich panels were used for the tests since this core has a high compressive strength, and resists in-plane stretching during panel bending [9, 35]. To ensure the compressive strain during the tests would be small, a core relative density, $\bar{\rho} = \rho_c/\rho_m$, of 30% was selected ($\rho_c$ is the smeared-out core density and ρ_m the material density of the stainless steel [30]). The honeycomb core density $\rho_c = \bar{\rho}\rho_m$ for a core made from 304 stainless steel with material density ρ_m = 7900 kg/m^3 was therefore 2370 kg/m^3. The sandwich panels were designed to have the same mass per unit area as the reference 304 stainless steel solid plates. Approximately a third of the solid plate mass was assigned to the core with the remainder distributed between the 7.9 mm thick front and 6.4 mm thick back face sheets. A slightly thicker impact face sheet was used to increase its bending resistance in the unsupported region between contacts with the core webs. Figure 4(a) shows a photograph of the core while Figure 4(b) and (c) show the top and section views of the square honeycomb core pattern. The sandwich panel design parameters are summarized in Table 1.

Table 1. The design parameters for the square honeycomb sandwich panels.

Cell width D (mm)	Web width t (mm)	Unit cell width l (mm)	Core height H_c (mm)	Front face thickness t_f (mm)	Back face thickness t_b (mm)	Panel thickness t_p (mm)	Corner radius r (mm)
44.45	6.35	50.80	36.50	7.90	6.40	50.80	9.50

The sandwich panels were fabricated from 1.32 m x 1.32 m x 7.6 cm thick 304 stainless steel plates that were first stress relieved at Rex Heat Treat (Warrendale, PA) at 538° C for eight hours and then machined at KVK Precision Technologies (Shenandoah, VA). This was the same steel and stress relief process used for the fabrication of the five solid (reference) test plates [34]. A 1.22 m x 1.22 m and 2.54 cm deep center pocket was first milled out of the plate to form a 5.08 cm wide picture frame outer edge. This allowed the panels to fit tightly over the test platform support base resulting in an edge restraint condition without interrupting subsequent flow of the granular particles over the impact surface. To avoid welding of the honeycomb core to the impact side face sheet of the sandwich panel, a 16 x 16 square array of 44.45 mm x 44.45 mm square cell pockets was milled in the center 81.3 cm x 81.3 cm square span of the panel. The centers of the cells were spaced 50.8 mm apart and each had a depth (i.e. core height, H_c) of

36.5 mm. To minimize stress concentrations, the corners and bottoms of the cell pockets were rounded to a 9.5 mm radius using a ball mill cutter as shown in Figure 4(b). The integral front (impact) face sheet was 7.9 mm thick. The integral face sheet/core structure had a total thickness ($H_c + t_f$) of 44.4 mm, Figure 4(a). A thinner 1.22 m x 1.22 m back face sheet with thickness t_b = 6.4 mm was then attached by electron beam welding at Sciaky, Inc. (Chicago, IL) to form the complete square honeycomb sandwich panel structure with a total thickness (panel height) of t_p = 50.8 mm.

A linear welding scan pattern in the orthogonal X- and Y- directions was adopted for welding at each of the honeycomb web and back face sheet intersections. Since the honeycomb cell matrix pattern was only defined in the center square 81.3 cm x 81.3 cm unsupported area, a series of additional perimeter welds were used to cover the area between the inner honeycomb cell matrix pattern and the outer picture frame edges, as shown in Figure 5. Electron beam weld parameters were first developed for the through thickness welding of small test coupons with a representative T-joint configuration consisting of a 6.4 mm thick face sheet and a 6.35 mm wide honeycomb web. This resulted in selection of an electron beam welding voltage of 50 kV and a 100 mA beam current with a travel speed 38.1 mm/s. The weld varied in width from 0.51 to 0.64 mm and had a total penetration depth of 10.16 mm. Since the back face sheet was 6.4 mm thick, the weld penetrated about 3.76 mm into the honeycomb core web. The use of a narrow weld width was necessary to avoid excessive thermal stress, and thus distortion of the panels. It is shown later that the rupture strength of these welds was insufficient to withstand the dynamic loading conditions of this test series.

2.3 Test charges

The five test charges were identical to those for the solid test plate study [34]. Their designs are summarized in Table 2. A carbon fiber reinforced polymer (CFRP) suspension rod, inserted through the center of the test charges during assembly, was used to assist in the suspension and alignment of the charges above the test panels. The three highest mass test charges (Shots 3-5) required the additional use of a net for their suspension. In order to create a similar impulse at the Kolsky bar to that at the plate center, the location of detonation on the explosive charge surface was inclined at $\theta = 45°$ from the test panel normal on the plane that contained the center axis of the Kolsky bar and test plate centerline, Figure 6. Positioning these heavy test charges in

an outdoor environment was challenging, and for the heaviest (~150 kg) test (Shot 5) it was difficult to achieve the desired detonation orientation, and so for this test the detonation location was $\theta = 49°$. After charge setup over the test panel, an instantaneous detonator (manufactured by Dyno Nobel, Inc. in Salt Lake City, Utah; model SP/SM (12-0)) was inserted into the explosive charge just prior to detonation.

Table 2. Charge configurations for the five sandwich panel test shots.

Test shot	Inner radius R_1 (mm)	Explosive mass (kg)	Outer radius R_2 (mm)	Annular shell width (mm)	Particle type	Particle mass (kg)	Water mass (kg)	Annular shell mass (kg)
1	80	3.0	152	72	Silica	19.30	4.36	23.66
2	80	3.0	203	123	Silica	51.92	12.58	64.50
3	90	4.5	203	113	Silica	50.24	11.88	62.12
4	90	4.5	203	133	ZrO_2	86.33	14.75	101.08
5	90	4.5	229	139	ZrO_2	126.88	22.05	148.93

The test charge centers were intended to be suspended a distance $H_p = 42.46$ cm above the top face of the sandwich panels and at an identical distance to the end of the Kolsky bar. However, prior to detonation, sufficient time elapsed for the test charges' positions to suffer small shifts in their locations. The high-speed video images of each test were therefore used to measure the exact standoff distances to the top of the test panels, H_p, and the front impact end of the Kolsky bar, H_k, at detonation. These are summarized in Table 3 together with the standoff distances for the reference solid plate tests.

Table 3. The standoff distance from the center of the test charge to the front face of the sandwich panel and Kolsky bar (the standoff distances to the solid plates for the reference test shots are listed [34]). The delay time for the Kolsky bar signal initiation and the impact time of the main sand front on the Kolsky bar are also listed.

Test shot	Standoff to Kolsky bar H_k (cm)	Standoff to sandwich panel H_p (cm)	Standoff to solid plate H_p (cm)	Signal delay time (μs)	Kolsky bar impact time (μs)
1	48.5	43.2	41.7	40	350
2	45.4	38.5	48.6	54	445
3	45.6	41.9	44.6	53	325
4	44.0	44.7	44.4	58	470
5	45.8	43.0	45.6	67	640

2.4 Kolsky bar

A strain gage instrumented, 3.81 m long, 2.54 cm diameter, age hardened, C-350 grade maraging steel Kolsky bar was used to measure the axial stress (pressure) and impulse-time response of the loading by granular impacts for the different test charge configurations. The Kolsky bar was positioned 42.46 cm above the front face sheet of the sandwich panel using four adjustable height pedestal supports to align the center of the Kolsky bar with the explosive charge center. The standoff distances from the charge center to the front of the Kolsky bar, H_k, was measured from the high-speed video images prior to detonation and are summarized in Table 3. The intent was to position the end of the Kolsky bar at an equivalent location to the center of the test panel top surface so that the applied pressure and impulse measured by the Kolsky bar represented the impact experienced by the test panel center. However, this proved to be challenging, and so the data collected from the Kolsky bar is used to evaluate the validity of the discrete simulations of each test. Once this validity was established, the code predicted impulse was used to establish the relationship between panel displacement and impulse.

Two T-rosette type strain gauges (Vishay Precision group, CEA-06-125UT-350) were mounted diametrically opposite each other and wired in a full Wheatstone bridge circuit 0.6 m from the front (impact) end of the Kolsky bar. The signal recorded by the strain gauges was used to calculate the axial stress (pressure) and applied impulse to the front of the bar by the granular media impacts. The strain gauge signal recording was initiated by the break of a trigger wire attached to the outer shell of the test charge. A time delay therefore existed between the moment of detonator excitation and the initiation of the signal recording. This delay time consisted of the time for a detonation wave to travel from the detonator to the C-4 explosive–granular matter interface, plus that for the resulting compressive shock front to propagate through the annular granular matter region and reach its outer surface. These delay times were obtained from simulations of each test, and varied from 40 μs to 67 μs, Table 3. For consistency, the start of detonation is defined as t = 0 s, and the Kolsky bar data from each test shot was therefore shifted by the calculated time taken for detonator excitation to cause rupture of the trigger wire on the external surface of the test charge. Table 3 also shows the time after detonation (determined from high-speed video image analysis) for the granular particle front to reach the front of the Kolsky

bar. Since the extensional wave speed in a C-350 steel bar is 4800 m/s, the time for a signal initiated by an impact at the front of the Kolsky bar to reach the strain gauge (located 0.6 m from the impacted end of the bar) was 125 μs. The 3.81 m length of the bar was selected to ensure that the signal measurement period of interest was not complicated by distal reflections, the first of which arrived 1.34 ms after the initial impact signal reached the strain gauge. We note that during Shot 2, the Kolsky bar data trigger signal failed to initiate recording of the data and the signal was not recorded.

3 Simulation methodology

3.1 Particle analysis

The five square honeycomb sandwich panel tests were numerically simulated using the IMPETUS Afea Solver [36]: a discrete particle based solver that models air, soil, and high explosive (HE) particles, and employs a corpuscular method to model particle interactions. Using a Lagrangian formulation, the solver fully couples the discrete particles with finite element (FE) models allowing interactions between the particles and structures to be simulated. A detailed description of the particle model and its implementation is given by Olovsson et al. [37] and Borvik et al. [38]. The simulations conducted here used the same methodology and particle collision parameters used for the analysis of the reference solid test plates [34]. A convergence study indicated that the use of 2 million simulation particles was sufficient to analyze each of the five tests. Because of the varying volume of the granular matter and high explosive for each test, the particle division between air, soil, and HE defined by the solver was slightly different for each simulation. These distributions are summarized for each simulated sandwich panel test in Table 4.

Table 4. Distribution of air, HE, and granular matter particles in the simulations for each test shot.

Test shot	Air particles	HE particles	Granular particles
1	849,692	707,078	443,230
2	617,878	508,193	873,929
3	556,265	688,240	755,495
4	557,828	684,505	757,667
5	468,104	586,956	944,940

3.2 FE geometry model

The test geometry that was modeled using the IMPETUS solver is shown in Figure 6. The experimental dimensions for the Kolsky bar, test rig support frame, and 5.08 cm thick square honeycomb sandwich panel as well as their positioning remained identical for the five tests that were modeled. Only the suspended charge configuration was varied for each simulation. The position of the charge center also varied from shot to shot (Table 3). The charges consisted of an inner spherical explosive and an outer annulus of water-saturated particles (fused silica or zirconia particles). The acrylic plastic shell with radius R_1 used to constrain the inner HE particles and a second outer acrylic shell of radius R_2 used to contain the annular region of granular matter were both modeled using a shell thickness of 3 mm. The spherical charge was suspended above the sandwich panel center with standoff distances to the test panel and Kolsky bar given in Table 3. To compare the displacements of the solid plates and the sandwich panels to the same test charge configuration, an additional set of simulations was performed using a fixed standoff distance (47.54 cm) to the back of both the solid plates and sandwich panels. The detonation was initiated on the surface of the HE sphere at the detonator location shown in Figure 6. For Shots 1-4, this was located at $\theta = 45°$ (measured from the test panel X-axis), while for Shot 5, $\theta = 49°$. A detailed description of the FE model for the Kolsky bar and test platform can be found in Kyner et al. [34].

The square honeycomb sandwich panel in Figure 6 was modeled as two separate parts. The integral front (impact side) face sheet and square honeycomb core were modelled as one part and the back face sheet as a second. The sandwich panel core consisted of an array of 16 x 16 honeycomb cells within the 81.3 cm x 81.3 cm unsupported center of the panel while the front face sheet was given a thickness of 7.9 mm. Each square honeycomb cell was 50.8 mm x 50.8 mm with a core depth, H_c, of 36.5 mm, shown in the inset of Figure 6. The back face sheet model used a 6.4 mm thickness. To enable weld line failure and debonding of the rear face sheet (as occurred in the experiments), it was initially connected to the honeycomb core panel using the merge option within the IMPETUS Afea solver [39]. The onset of this debonding during a test was found to be weakly influenced by the merge failure force selected. The force failure criterion of 0.25 MN used was determined from the area of a weld line (81.3 cm x 0.1 cm) multiplied by the yield stress (310 MPa) of the stainless steel. A refined mesh was used in the

40.6 cm x 40.6 cm center region of the honeycomb core where panel deformation was most severe. The sandwich panel FE model had a total of 188,816 linear hexahedra elements and 253,290 nodes. The full FE model (Kolsky bar, test support base, bolts, acrylic spherical shells, and honeycomb sandwich panel) consisted of 230,728 elements (432 linear pentahedra and 230,296 linear hexahedra elements) with 1,352,484 nodes.

The same Johnson-Cook parameters used in the reference solid plate study [34] were used to define the material properties for the 304 stainless steel honeycomb panels [40, 41], the A-36 test support frame [42], the C-350 grade age hardened, maraging steel Kolsky bar [43, 44], and the four carbon steel bolts that attached the panel to the support structure [45]. There was no fracture of the honeycomb panels or cells observed after testing. Therefore, a damage failure model was not included in the simulations other than that associated with the use of the back face merge failure criteria.

4 Results and Discussion

4.1 Granular front propagation

The high-speed video observations of the radial granular particle shell expansions are shown in Figure 7 for test Shots 1-3 (fused silica particles) and in Figure 8 for test Shots 4 and 5 (zirconia particles). For consistency with simulations and Kolsky bar measurements, $t = 0$ s is defined as the moment of detonation for all tests. The images show the initial configuration and those at approximately 250 and 650 μs after detonation. They were consistent with previous observations for the similar series of tests conducted with the reference solid plates [34]. Examination of the first and second columns of Figure 7 shows that an increase in mass of the fused silica particles in the annular region around the explosive charge, while keeping the explosive mass fixed, resulted in a decrease in the radial expansion rate of the granular particle (sand) front. Examination of the second and third columns in Figure 7 reveals that the expansion rate increased when the explosive mass was increased from 3 to 4.5 kg while the silica particle mass remained fixed. A sand fingering effect, evident in the insets of Figure 7(c), (f), and (i), developed at the leading edge of the highest radial velocity tests (Shots 1 and 3). These sand fingers were also observed in the reference study and were attributed to an instability at the sand/air interface recently analyzed by Kandan et al. [46].

Comparison of Shot 3, Figure 7(g)-(i) with Shot 4, Figure 8(a)-(c) illustrates the effect of replacing fused silica particles with higher density, and therefore greater mass, zirconia particles while keeping both the explosive charge mass (4.5 kg) and volume of granular matter fixed. The increase in granular particle mass resulted in a reduction of the radial expansion velocity of the particle front, consistent with the transfer of a fixed momentum from the HE particles. A further increase of zirconia particle mass by increasing the outer shell radius of R_2 from 203 to 229 mm resulted in a further reduction of granular particle velocity, and gradual disappearance of particle front fingering. The impact times for the main sand front (the region from which the sand fingers emerged) against the front of the Kolsky bar for each test shot are summarized in Table 3. It is also noted that while the wide plastic flange around the spherical test charge clearly reduced the sand front expansion in its radial direction, the orientation of all the test charges was such that it had no effect on the loading of the Kolsky bar or sandwich panels.

The high-speed video observations show only the outer sand front expansion and the developing sand fingers. However, the particle-based simulations allow assessment of both the particle front propagation and the particles behind the leading sand front during its radial expansion. Figure 9 shows examples of such simulations for the fused silica particle tests (Shots 1-3), while Figure 10 shows analogous results for the zirconia particle tests (Shots 4 and 5). The first three rows of results in Figure 9 show the particle positions at detonation and two times after detonation that correspond to those of the high-speed video images in Figure 7. Consistent with the experimental observations discussed above, the leading edge particle expansion velocity is seen to decrease (from Shot 1 to 2) with increased granular mass and increase (from Shot 2 to 3) as the explosive charge mass was increased. These changes in the particle expansion velocity are clearly seen in the third row of images in Figure 9 at 650 μs after detonation at which time the sandwich panel had begun to deform. The slower expansion of the zirconia particle test shots observed with the high-speed video imaging is also evident in the simulated results shown in Figure 10. Comparison of Figure 9(c, g, and k) with Figure 10(c and g) show that the lower particle front expansion rate of the zirconia particle tests delayed the start of panel deformation. The bottom row of results in Figure 9 and Figure 10 show the panel deformations at 2 ms after detonation at which time the granular (sand) and HE particles have dispersed, and elastic oscillations of the panels have decayed.

The simulations reveal that as the granular particle shells expanded, particle velocity and density gradients developed within the expanding annular granular particle region. A densified region of air (not shown) also developed in front of the expanding sand particles. The development of this air shock was recently shown to result from momentum transfer from granular matter particles to the background air particles during their collisions near the granular particle front [25]. A region of fast, low density particles can be seen at the outer edge of the expanding sand front in Figure 9 (at the air/sand interface) which is correlated with the sand figures in Figure 7. These fast particles are followed by a main sand front of increased density and trailed by a region of dense, low velocity particles pushed outward by the expanding HE particles. This low velocity annular ring of high particle density can be clearly seen in Figure 9(g) at t = 650 μs. Figure 9(c) shows that the first particles that impacted the panel accumulated on the surface forming a higher particle density region above the plate surface. These particles were then displaced laterally outwards along the panel surface by later arriving particles, Figure 9(c). At this time, impact of the sand particles with the honeycomb sandwich panel can be observed and panel deformation had begun. These three regions of particle density and velocity were also present in the zirconia simulations Figure 10. However, there was much less particle dispersion, consistent with a less prominent sand fingering effect seen in Figure 8(c) and (f).

4.2 Kolsky bar responses

The impact loading response of the Kolsky bar for each test shot was measured using strain gauges located 0.6 m from the impact end of the bar, and are presented as Figures A1 and A2 in the Appendix. The time-integrated pressures gave the measured impulse transmitted to the bars, and these are also shown in Figures A1 and A2. The particle based simulation method was also used to predict the impulse versus time response, and these waveforms are shown for each test in the figures. The impulse responses were very similar to those previously reported [34] for studies of the reference solid plate response to the same test charge configurations. The impulse waveforms exhibited four loading regimes. The reader is referred to the previous study [34] for a detailed discussion of the four regimes of loading shown in Figures A1 and A2. Briefly, Region I corresponded to the beginning of the impact process. It was shown in the previous study [34] to corresponded to the arrival of the fastest granular particles associated with the fingering instability. Region II was associated with the arrival of the main granular particle

front. Region III corresponded to the arrival of the slowest velocity, but highest density granular particle region that was "pushed" by the expanding explosive detonation product particles, while Region IV covered the time when only detonation product particles were incident upon the bar. The measured and simulated plateau impulse values are summarized in Table 5. In general, the simulations were in good agreement with the experimental results, giving confidence in the simulated impulse applied to the panel directly beneath the test charge (the simulated panel impulse value in Table 5). Table 5 also shows the predicted impulses (applied directly beneath the test charges) to the reference solid plate tests of the earlier study [34]. They were usually smaller than those of the comparable sandwich panel tests since the solid plate impact face was 2.54 cm further from the test charge center. However, Table 3 shows that motion of the charges prior to detonation resulted in varied standoff distances due to the difficulty of maintaining the intended standoff distance. As a result, the impulses applied to the solid and sandwich panels for each of the five test shot conditions were different.

Table 5. Experimental and simulated impulse (plateau) applied to the Kolsky bar as well as the simulated peak impulse applied to the sandwich panels. The simulated peak impulses applied to the solid reference plates is also listed [34].

Test shot	Experimental Kolsky bar impulse (kPa·s)	Simulated Kolsky bar impulse (kPa·s)	Simulated panel impulse (kPa·s)	Simulated solid plate impulse (kPa·s)
1	8.7	8.9	17.6	15.3
2	NA	14.6	26.1	16.5
3	19.5	19.4	28.3	22.4
4	21.7	21.1	31.7	24.2
5	23.1	22.5	33.7	25.4

4.3 Panel deflection

A coordinate measuring machine (Zeiss Prismo Vast) was used to measure the out of plane (Z-direction) surface profile of the top (impact) face of the sandwich panels. Contour plots of the permanent Z-component displacement are shown for the sandwich panels in Figure 11 for the fused silica particle test shots and Figure 12 for the zirconia particle test shots. The simulated panel contour plots at 20 ms after detonation are also shown for comparison. At this time, the oscillatory response of the test panels had sufficiently decayed to enable determination of the permanent (plastic) displacement. The 81.3 cm x 81.3 cm center region occupied by the honeycomb cells is indicated on all the images. The 40.6 cm x 40.6 cm region near the panel

center where a refined mesh was utilized is also shown on Figure 11(d) and Figure 12(c). For consistency, the same 0-8.0 cm Z-direction permanent displacement scale is used for all plots. The maximum measured and simulated permanent Z-direction displacements of the panels are summarized in Table 6. The panel (front face) deflections, δ_f, increased from Shot 1 to Shot 5, consistent with an increase in the impulse applied to the test panels. All the simulated maximum displacements were within 15% of the measured the values.

Table 6. The permanent Z-displacement of the sandwich panels.

Test shot	Experimental front face displacement δ_f (cm)	Simulated front face displacement δ_f (cm)	Experimental back face displacement δ_b (cm)	Difference in face sheet displacements $\Delta\delta$ (mm)
1	3.32	3.65	3.37	-0.5
2	5.50	6.33	5.20	3.0
3	6.35	7.23	5.90	4.5
4	7.21	7.28	6.93	2.8
5	8.17	8.24	7.49	6.8

The electron beam welds securing the back face sheet to the square honeycomb sandwich panel core failed during every test, and the back face sheet debonded from the core. The simulations indicated this failure occurred very early in the loading process during reflection of the first plastic shock front to arrive at the core web - rear face sheet interface. The final permanent deflection of the (debonded) back face sheet, δ_b, was also measured and is recorded in Table 6. The displacement of the panel front face was usually a little larger than that of the rear face. The difference between the Z-direction displacements of the front and back face sheets, $\Delta\delta = \delta_f - \delta_b$, is therefore also summarized in Table 6. The difference in front and back face sheet displacements could have resulted from compression of the square honeycomb core. The final core height of the panels in the region of maximum panel deflection (an average of the four webs at this maximum deflection location) was measured after testing (since the back face sheets were no longer attached) and are summarized in Table 7. They show that the permanent compression of the core was substantially less than the difference in displacements of the front and rear faces, consistent with detachment of the rear face sheet before maximum panel bending was attained. Both the measured and simulated core compressions, ΔH_c increased with impulse reaching a maximum of approximately 2 mm, Table 7 together with the core plastic compressive

strain $\varepsilon_c = \Delta H_c/H_c$ (where the initial core height was H_c = 36.5 mm) . The measured core strains reached a maximum of 5.88 ± 1.19% for the highest impulse test. The simulated strains exhibited a similar trend with test shot number. The small core compressive strains are consistent with the high compressive strength of the square honeycomb core [11].

Table 7. Measured and simulated core compression and the compressive strain for each test shot in the region of maximum panel deflection.

Test shot	Measured core compression ΔH_c (mm)	Simulated core compression ΔH_c (mm)	Measured core compressive strain ε_c (%)	Simulated core compressive strain ε_c (%)
1	0.40 ± 0.4	0.65	1.12 ± 1.12	1.78
2	0.79 ± 0.4	0.95	2.27 ± 1.15	2.60
3	1.19 ± 0.4	1.09	3.45 ± 1.16	2.99
4	1.59 ± 0.4	1.26	4.65 ± 1.17	3.45
5	1.98 ± 0.4	1.38	5.88 ± 1.19	3.78

While the Kolsky bar measures of pressure and impulse are close to those applied to the center of the test panels during the event, the shifts in the test charge location prior to detonation meant they were not the same. However, since the measured and predicted impulses applied to the Kolsky bars were similar, the impulse applied to the test panels by simulations that used the correct charge center locations (obtained from high-speed video image analysis, Table 3) could be used to compute the impulse distributions on the test panels. Figure 13 shows the impulse distribution on half sections of the honeycomb sandwich panels and the panel cross section deflection for the five test shots. These results show the impulse applied to the panels was most strongly distributed over a central, 40 cm wide region of the panels and that the panel deflection increased with impulse. The impulse applied to the sandwich panels was approximately the same as the incident impulse indicating a negligible FSI effect during these tests.

The simulated axial plastic strains in the X and Y directions, ε_{XX} and ε_{YY}, (determined at 20 ms after detonation) for the top surface of the sandwich panel have been superimposed on the sandwich panel for test Shot 3 and are shown in Figure 14. The greatest strain is seen to have occurred above the inner edge of the steel picture frame support (the area containing the square honeycomb sandwich panel). The majority of this strain was within the unsupported 81.3 cm span of the honeycomb panel with only a small amount of in-plane plastic "pull-in" strain extending outwards beyond the underlying edge grip location. This indicates stretching of

material outside the grip location contributed little to the final permanent displacement of the sandwich panels. Instead, the panel deflection was accommodated by stretching of the face sheets and the webs of the square honeycomb core.

Figure 15 shows the dimensionless deflection at the center of the front face of the sandwich panels as a function of the dimensionless impulse applied to their impact face, and compares this with the response of the reference solid plates [34]. Figure 15(a) shows the simulated maximum total (elastic and permanent) deflection determined directly below the center of each test charge while Figure 15(b) shows the permanent deflection of the panels (measured and simulated). In both cases, the deflections are normalized by the half span L (where 2L = 81.3 cm) of the unsupported region occupied by the square honeycomb sandwich. The dimensionless impulse, $I_o/\mathrm{m_b}\sqrt{\sigma_\mathrm{Y}/\rho_\mathrm{m}}$, was determined from the simulations where I_o corresponds to the maximum impulse applied to the sandwich panels directly beneath each charge. For each test shot, I_o is listed in Table 5. For the dimensionless impulse, I_o is scaled by the areal mass of the sandwich panels ($\mathrm{m_b} = \rho_\mathrm{m} t_f + \rho_\mathrm{m} t_b + \rho_c H_c$ = 199.5 kg/m^2) or the solid plates, and the plastic wave speed of the alloy (the square root of the ratio of panel material yield strength σ_Y = 310 MPa and density ρ_m = 7900 kg/m^3). The simulations permitted rear face sheet debonding during the tests, which occurred at an early stage of the test event.

Results for each pair of tests (i.e. solid and sandwich panel subjected to the same test shot type) are indicated by numbers (1 to 5) adjacent to the data points. Since the solid plates were thinner than the sandwich, their front faces were intended to be further from the test charge center and should therefore experience a smaller impulse than their sandwich panel counterparts (Figure 3). However, Table 3 gives the actual standoff distances for both sets of tests, and indicates that small drifts in test charge location during both test series resulted in significant variations of the standoff distance. As a result for some test shots, the impulses applied to the solid plates and sandwich panels differed by more than that due to the difference in sample thickness. Additional simulations were therefore performed in which the distance from the charge center to the rear target surface was fixed at 47.54 cm so the sandwich panels all experienced identical applied impulses. Similarly, simulations were performed with the solid plates fixed at the 47.54 cm standoff distance to the back face. Simulations using smaller explosive and silica particle masses that resulted in lower impulses than the experiments were

also conducted for both test panel types (using a fixed standoff distance of 47.54 cm to the back face sheet) to predict the low impulse behavior.

The results in Figure 15(a) indicate that the maximum dynamic deflection from an impulsive granular matter impact event scales linearly with impulse. Since data for both spherical silica and angular zirconia particle impacts can be fitted to the same linear relation, we infer that the dynamic deflection of both the solid plates and sandwich panels was only modestly affected by particle density or particle shape. It is also evident that the use of a strong core sandwich panel with a panel thickness to half-span ratio of approximately 1/8, reduces the dynamic deflection by approximately 30% when the front faces were subjected to the same impulse compared as the reference solid plate. However, since the front (impact) face of the honeycomb sandwich panels was located 2.54 cm closer to the center of the test charges than the top surface of the solid test plates, the sandwich panels experienced a higher impulse compared to the solid test plates tested with the same five charge configurations. The sandwich panel benefit was therefore offset by the increase in impulse applied to the sandwich panel front face.

The permanent displacement of the front face sheet of the sandwich panel is plotted versus incident impulse at the panel center in Figure 15(b) and again compared to results for the reference solid plates. Both the measured displacements (solid data points) and simulated results (open data points) for the test conditions are shown. Examination of Figure 15(b) shows that when the sandwich panel was subjected to the same test as a solid plate, the sandwich panel permanent deflection was reduced.

Since the variations in actual standoff distances were significant for pairs of tests, simulations were conducted using the intended standoff distance to the back face (47.54 cm) for each specimen type (solid plate and honeycomb sandwich panel). The dimensionless maximum dynamic and permanent deflections for both the solid and sandwich panels are shown in Figure 16(a) and (b). These are plotted versus the dimensionless impulse applied to the solid plates simulated at a fixed standoff distance, and each shot number is indicated above the simulated data points. At lower levels of impulse, the deflections of the sandwich panels were significantly less than those of the solid plate. As the impulse applied to the panels increased, the dynamic and permanent displacements of the solid plates and sandwich panels tested under similar conditions

(same test numbers) converged, consistent with a loss of the sandwich panels bending stiffness as out of plane displacements exceeded the panel thickness.

The electron beam welds that attached the back face sheet to the sandwich panel core failed during experimental testing and were completely detached from the rest of the test structure. The simulation methodology used to obtain the results above had modeled this back face sheet connection using a merge failure criterion (Section 3). To examine the effect of back face sheet debonding criterion on the sandwich panel deformation, two other bonding conditions were simulated. One set of simulations modeled the back face using a fully bonded interfacial criterion that did not permit failure. This is referred to as the bonded simulation. The other case never connected the back face sheet to the core, and this is referred to as the non-bonded condition. This geometry was therefore equivalent to that of a waffle-stiffened panel placed upon an unattached metal sheet. The maximum dynamic deflection of the sandwich panels using these two additional back face attachment conditions are shown as a function of the dimensionless applied impulse for the five tests in Figure 15(c), and compared with the results from Figure 15(a) for the merged failure attachment condition. For each test shot, the bonded sandwich panel (in which no weld failure occurred) slightly outperformed the debonded panel where a merge failure was used to simulate the weld failure during loading (as observed in the experimental testing). Conversely, the simulations of tests that used a non-bonded back face sheet (in which the back face sheet was never attached to the sandwich panel core) resulted in slightly larger deflections than for the debonded case where failure occurred during the test. These results indicate that simpler to manufacture waffle-stiffened panels may perform almost as well as the sandwich.

5 Concluding Remarks

This study has analyzed the impact of explosively accelerated fused silica and zirconia granular matter against a 304 stainless steel, square honeycomb sandwich panel with a mass per unit area of 199.5 kg/m^2. The test charges were designed to create approximately spherical expanding shells of granular matter. High-speed video techniques were used to image the leading edge of the expanding shells and showed that their radial velocity could be varied from 500-1,200 m/s by reducing the granular matter to explosive mass ratio. A Kolsky bar was used to

determine the pressure and impulse applied by the impact of the granular matter at a location equivalent to that of the panel centers. A previously validated discrete particle simulation code was used to simulate the tests and successfully predicted the measured Kolsky bar responses and radial expansion rates of the expanding granular fronts. The simulated out of plane permanent displacement of the five sandwich panels was also in good agreement with the measured displacements.

The five panels' out of plane (simulated) dynamic and (measured and simulated) permanent displacement were compared to a previous study in which identical test charge configurations were used to load equivalent mass per unit area solid plates of the same alloy. The study sought to maintain a fixed standoff distance from charge center to the rear surface of the test plates/panels. As a result, the impact front face of the thicker sandwich panels was 2.54 cm closer to the test charge center than the equivalent (mass and material) solid plate, and experienced a higher impulsive load compared to the solid plate. Even so, the study indicated a substantial reduction of deflection when sandwich panels were used, provided the sandwich panel deflection did not significantly exceed the thickness of the panel. The benefit of the sandwich panel design therefore decreased as the impulse increased. Even though the rear face sheet of the sandwich panel debonded early in the loading process, the majority of the flexural strength of the panel design was retained during impact. The reduced sandwich panel deflections were consistent with this retained flexural strength and no significant change of impulse by fluid structure interactions was observed in this study.

Acknowledgements

The authors are very grateful for the experimental assistance of Tommy Eanes. This research was funded by the Defense Advanced Research Projects Agency (DARPA) under grant number W91CRB-11-1-0005 (Program manager, Dr. J. Goldwasser).

Appendix

The instrumented Kolsky bar was used to measure the applied pressure and impulse by granular media impacts to represent the loading experienced by the square honeycomb sandwich panels. The five charge configurations were almost identical to those used and then

characterized for the testing on the reference solid plates [34]. The measured pressure-time waveforms and impulse-time responses are shown in Figure A1 for the fused silica particle test shots (Shots 1 and 3) and Figure A2 for the zirconia test shots (Shots 4 and 5). The strain gauge signal corresponds to particle impacts that occurred 125 μs earlier on the front of the bar. Kolsky bar data was not recorded for test Shot 2 in this test series. Examination of each of the pressure-time signals revealed several distinct characteristics which correspond to four distinct regions of granular particle loading observed in the impulse-time response. Initial impacts resulting in an initial small pressure pulse, followed by small waveform oscillations to a much larger pressure peak resulting from impact by the densest particle region. These observations are consistent with those previously made for the same five charge configurations (Shots 1-5) that were tested on the solid plates [34]. The four regions of impulse loading are indicated in Figure A1(b) and Figure A2(b) and are briefly discussed here with more details described by Kyner et al. [34].

The initial small pressure pulse correlates to an initial bump in impulse (Region I) that corresponds to initial impacts by the fastest, low density sand particles (the sand fingers observed in the high-speed videos). Since there is not a prominent sand fingering effect at the leading edge of the sand front for the zirconia test shots, the main sand front impact corresponds to the initial Region I impact. This is followed by a sloped region of slowly increasing impulse (Region II). The start of Region II correlates to the impacts of the main sand front recorded in Table 3 for the fused silica particle test Shots 1-3. This period of gradually increasing impulse of Region II is followed by a sharp jump in impulse (Region III) at the arrival time of the pressure peak. Simulations reveal that this jump in impulse is a result of impacts by the low velocity, high density trailing granular particles. Impacts by the detonation products directly follow but contribute very little additional impulse as the impulse reaches a plateau value in Region IV.

References

[1] T. Ngo, P. Mendis, A. Gupta, J. Ramsay, Blast loading and blast effects on structures–an overview, Electronic Journal of Structural Engineering, 7 (2007) 76-91.
[2] A. Anusree, A.M. Biju, A.S. EK, D. Remesh, K. Rinsa, Effect of Blast Loading on Columns: A Critical.
[3] F. Zhu, G. Lu, A review of blast and impact of metallic and sandwich structures, EJSE Special Issue: Loading on Structures, 92 (2007) 101.
[4] H. Hao, Y. Hao, J. Li, W. Chen, Review of the current practices in blast-resistant analysis and design of concrete structures, Advances in Structural Engineering, 19 (2016) 1193-1223.
[5] C.E. Anderson, T. Behner, C.E. Weiss, Mine blast loading experiments, International journal of impact engineering, 38 (2011) 697-706.
[6] I. Cullis, Blast waves and how they interact with structures, Journal of the Royal Army Medical Corps, 147 (2001) 16-26.
[7] G. Taylor, The pressure and impulse of submarine explosion waves on plates, The scientific papers of GI Taylor, 3 (1963) 287-303.
[8] R. Cole, Underwater explosions, Princeton University Press, Princeton, NJ, 1948.
[9] Z. Xue, J.W. Hutchinson, A comparative study of impulse-resistant metal sandwich plates, International journal of impact engineering, 30 (2004) 1283-1305.
[10] Y. Liang, A.V. Spuskanyuk, S.E. Flores, D.R. Hayhurst, J.W. Hutchinson, R.M. McMeeking, A.G. Evans, The response of metallic sandwich panels to water blast, Journal of Applied Mechanics, 74 (2007) 81-99.
[11] H. Rathbun, D. Radford, Z. Xue, M. He, J. Yang, V. Deshpande, N. Fleck, J. Hutchinson, F. Zok, A. Evans, Performance of metallic honeycomb-core sandwich beams under shock loading, International Journal of Solids and Structures, 43 (2006) 1746-1763.
[12] K.P. Dharmasena, H.N. Wadley, K. Williams, Z. Xue, J.W. Hutchinson, Response of metallic pyramidal lattice core sandwich panels to high intensity impulsive loading in air, International journal of impact engineering, 38 (2011) 275-289.
[13] K.P. Dharmasena, H.N. Wadley, Z. Xue, J.W. Hutchinson, Mechanical response of metallic honeycomb sandwich panel structures to high-intensity dynamic loading, International journal of impact engineering, 35 (2008) 1063-1074.
[14] Z. Wei, K. Dharmasena, H. Wadley, A. Evans, Analysis and interpretation of a test for characterizing the response of sandwich panels to water blast, International journal of impact engineering, 34 (2007) 1602-1618.
[15] K. Dharmasena, D. Queheillalt, H. Wadley, P. Dudt, Y. Chen, D. Knight, A. Evans, V. Deshpande, Dynamic compression of metallic sandwich structures during planar impulsive loading in water, European Journal of Mechanics-A/Solids, 29 (2010) 56-67.
[16] N. Fleck, V. Deshpande, The resistance of clamped sandwich beams to shock loading, Journal of Applied Mechanics, 71 (2004) 386-401.
[17] J.W. Hutchinson, Z. Xue, Metal sandwich plates optimized for pressure impulses, International Journal of Mechanical Sciences, 47 (2005) 545-569.
[18] H. Wadley, K. Dharmasena, Y. Chen, P. Dudt, D. Knight, R. Charette, K. Kiddy, Compressive response of multilayered pyramidal lattices during underwater shock loading, International journal of impact engineering, 35 (2008) 1102-1114.

[19] Z. Wei, V. Deshpande, A. Evans, K. Dharmasena, D. Queheillalt, H. Wadley, Y. Murty, R. Elzey, P. Dudt, Y. Chen, The resistance of metallic plates to localized impulse, Journal of the Mechanics and Physics of Solids, 56 (2008) 2074-2091.
[20] N. Kambouchev, L. Noels, R. Radovitzky, Nonlinear compressibility effects in fluid-structure interaction and their implications on the air-blast loading of structures, Journal of Applied Physics, 100 (2006) 063519.
[21] J.W. Hutchinson, Energy and momentum transfer in air shocks, Journal of Applied Mechanics, 76 (2009) 051307.
[22] V. Aune, E. Fagerholt, K. Hauge, M. Langseth, T. Børvik, Experimental study on the response of thin aluminium and steel plates subjected to airblast loading, International journal of impact engineering, 90 (2016) 106-121.
[23] A. Vaziri, J.W. Hutchinson, Metal sandwich plates subject to intense air shocks, International Journal of Solids and Structures, 44 (2007) 2021-2035.
[24] R.L. Holloman, V. Deshpande, H.N.G. Wadley, Impulse transfer during sand impact with a solid block, International journal of impact engineering, 76 (2015) 98-117.
[25] A. Kyner, K. Dharmasena, K. Williams, V. Deshpande, H. Wadley, High intensity impulsive loading by explosively accelerated granular matter, International Journal of Impact Engineering, 108 (2017) 229-251.
[26] T. Liu, N. Fleck, H. Wadley, V. Deshpande, The impact of sand slugs against beams and plates: Coupled discrete particle/finite element simulations, Journal of the Mechanics and Physics of Solids, 61 (2013) 1798-1821.
[27] K.P. Dharmasena, H.N. Wadley, T. Liu, V.S. Deshpande, The dynamic response of edge clamped plates loaded by spherically expanding sand shells, International journal of impact engineering, 62 (2013) 182-195.
[28] R.L. Holloman, V. Deshpande, H.N.G. Wadley, Impulse transfer during sand impact with a cellular structure, International journal of impact engineering, 82 (2015) 36-58.
[29] H.N. Wadley, T. Børvik, L. Olovsson, J.J. Wetzel, K.P. Dharmasena, O.S. Hopperstad, V. Deshpande, J.W. Hutchinson, Deformation and fracture of impulsively loaded sandwich panels, Journal of the Mechanics and Physics of Solids, 61 (2013) 674-699.
[30] H.N. Wadley, Multifunctional periodic cellular metals, Philosophical Transactions of the Royal Society of London A: Mathematical, Physical and Engineering Sciences, 364 (2006) 31-68.
[31] H.N. Wadley, N.A. Fleck, A.G. Evans, Fabrication and structural performance of periodic cellular metal sandwich structures, Composites Science and Technology, 63 (2003) 2331-2343.
[32] F.W. Zok*, H. Rathbun, M. He, E. Ferri, C. Mercer, R.M. McMeeking, A.G. Evans, Structural performance of metallic sandwich panels with square honeycomb cores, Philosophical Magazine, 85 (2005) 3207-3234.
[33] F. Cã, B.P. Russell, V.S. Deshpande, N.A. Fleck, The through-thickness compressive strength of a composite sandwich panel with a hierarchical square honeycomb sandwich core, Journal of Applied Mechanics, 76 (2009) 061004.
[34] A. Kyner, K. Dharmasena, K. Williams, V.S. Deshpande, H.N.G. Wadley, High intensity impact of granular matter with edge-clamped ductile plates, International journal of impact engineering, (2017).
[35] D. Radford, G. McShane, V. Deshpande, N. Fleck, Dynamic compressive response of stainless-steel square honeycombs, Journal of Applied Mechanics, 74 (2007) 658-667.

[36] A.G. Hanssen, L. Olovsson, Welcome to IMPETUS AFEA, in, IMPETUS AFEA, Flekkefjord, Norway.
[37] L. Olovsson, A.G. Hanssen, T. Børvik, M. Langseth, A particle-based approach to close-range blast loading, European Journal of Mechanics - A/Solids, 29 (2010) 1-6.
[38] T. Børvik, L. Olovsson, A. Hanssen, K. Dharmasena, H. Hansson, H. Wadley, A discrete particle approach to simulate the combined effect of blast and sand impact loading of steel plates, Journal of the Mechanics and Physics of Solids, 59 (2011) 940-958.
[39] A.G. Hanssen, L. Olovsson, Command Manuel, in, IMPETUS Afea, 2017.
[40] J. Dean, C. Dunleavy, P. Brown, T. Clyne, Energy absorption during projectile perforation of thin steel plates and the kinetic energy of ejected fragments, International journal of impact engineering, 36 (2009) 1250-1258.
[41] L. Mori, S. Lee, Z. Xue, A. Vaziri, D. Queheillalt, K. Dharmasena, H. Wadley, J. Hutchinson, H. Espinosa, Deformation and fracture modes of sandwich structures subjected to underwater impulsive loads, Journal of mechanics of materials and structures, 2 (2007) 1981-2006.
[42] E.L. Guzas, C.J. Earls, Simulating blast effects on steel beam-column members: Methods, Computers & Structures, 89 (2011) 2133-2148.
[43] J.D. Cinnamon, A.N. Palazotto, Z. Kennan, Material characterization and development of a constitutive relationship for hypervelocity impact of 1080 Steel and VascoMax 300, International journal of impact engineering, 33 (2006) 180-189.
[44] U.K. Viswanathan, R. Kishore, M.K. Asundi, Effect of thermal cycling on the mechanical properties of 350-grade maraging steel, MMTA, 27 (1996) 757-761.
[45] G. Cohen, P. Gilles, S. Segonds, M. Mousseigne, P. Lagarrigue, Thermal and mechanical modeling during dry turning operations, The International Journal of Advanced Manufacturing Technology, 58 (2012) 133-140.
[46] K. Kandan, S.N. Khaderi, H.N.G. Wadley, V.S. Deshpande, Surface instabilities in shock loaded granular media, Journal of the Mechanics and Physics of Solids, 109 (2017) 217-240.

Figure Captions

Figure 1. (a) Edge clamped monolithic plate and (b) sandwich panel impacted by a sand slug at normal incidence. (c) Discrete particle predictions of the dimensionless maximum (elastic plus plastic) dynamic deflection of the monolithic plate and two sandwich panels with differing normalized core strengths ($\bar{\sigma}_c$) versus dimensionless impulse. (Adapted from Liu et al. [26])

Figure 2. Sandwich panel test setup showing the location of the spherically suspended test charge, the edge restrained sandwich panel, and the strain gage instrumented Kolsky bar used for impulse measurements.

Figure 3. Schematic diagram showing the test arrangement for edge clamped solid plate (left) and equivalent square honeycomb sandwich panel (right). The standoff distance from test charge center to the back face of the solid plate and sandwich panel, H_b, was intended to remain constant for the experimental tests. The standoff distance, H_p, to the target front faces was 2.54 cm smaller for the sandwich due to its greater thickness.

Figure 4. (a) A photograph of the square honeycomb core sandwich panel before the back (bottom) face sheet was attached. The square honeycomb pockets were machined from a thick plate so that the impact side face sheet did not require bonding with the core structure. (b) Shows a schematic view of the cells viewed from above. (c) Shows a schematic illustration of the connection between the front face sheet and the core webs.

Figure 5. The linear electron beam welding pattern used for attachment of the back face sheet. Each weld line penetrated the back face sheet and center of each honeycomb web to a depth of 3-4 mm. Additional weld lines were used to attach the back face sheet to the 20.3 cm wide solid panel region outside the honeycomb core.

Figure 6. Cross section of the model geometry used for simulations of the tests with an inset showing the mesh used for the honeycomb core and back face sheet.

Figure 7. Fused silica microsphere tests with square honeycomb sandwich panels showing approximately equivalent time snapshots for Shot 1 (R1 = 80 mm; R2 = 152 mm; 3 kg explosive charge), Shot 2 (R1 = 80 mm; R2 = 203 mm; 3 kg explosive charge), and Shot 3 (R1 = 90 mm; R2 = 203 mm; 4.5 kg explosive charge).

Figure 8. Zirconia particle tests with square honeycomb sandwich panels showing approximately equivalent time snapshots for Shot 4 (R1 = 90 mm; R2 = 203 mm; 4.5 kg explosive charge) and Shot 5 (R1 = 90 mm; R2 = 229 mm; 4.5 kg explosive charge).

Figure 9. Simulated sand front propagation for the three fused silica particle tests (Shots 1-3) for t = 0 s (the moment of detonation), t = 250 μs, t = 650 μs, and t = 2 ms. The silica particles are tan while the inner red particles are those of the high explosive.

Figure 10. Simulated sand front propagation of the two zirconia particle tests (Shots 4 and 5) for t = 0 s (the moment of detonation), t = 250 μs, t = 650 μs, and t = 2 ms. The zirconia particles are tan and the high explosive particles are red.

Figure 11. Test panel permanent plastic displacement contour plot in the Z direction for the silica particle tests (Shots 1-3). Experimental profilometry measurements are shown in (a), (b) and (c). These measurements did not include the outer edge (white region) of the panels. The corresponding simulated responses (evaluated at t = 20 ms) are shown in (d), (e), and (f). The 81.3 cm wide black square indicates the edge of the underlying support base and location of the region with honeycomb cells. The inner, 40.6 cm wide black box indicates the refined mesh region used in the FE model. The 122 mm wide dashed white box in the simulation plots indicates the position of the edge grip from which displacements were determined.

Figure 12. Test panel permanent plastic displacement contour plot in the Z direction for the zirconia particle tests (Shots 4 and 5). Experimental profilometry results are shown in (a) and (b). The simulated responses (at t = 20 ms) are shown in (c) and (d).

Figure 13. The cross section of the simulated square honeycomb sandwich panels showing the predicted specific impulse distribution applied to the surface by the five test shots. The 81.3 cm wide (unsupported) region of the honeycomb core sandwich section is indicated along with the 40.6 cm wide center region where a refined mesh was used. The predicted permanent deformation and permanent out of plane deflection (δ) is also shown for each test.

Figure 14. Superposition of the in-plane extensional strains (ε_{XX} and ε_{YY}) on the top face of the honeycomb sandwich panel for Shot 3 after an elapsed time t = 20 ms. The dotted white box indicates the location of the 122 cm wide edge grip.

Figure 15. (a) The simulated peak dynamic displacement at the center of the sandwich panels and reference solid plates versus the applied impulse. The numbers adjacent to some data points correspond to the test shot number. The simulations permitted rear face sheet debonding during the impulsive loading of the sandwich panel. (b) The measured and simulated permanent front face displacement at the center of the test structures versus the applied impulse. The sandwich panel simulations again allowed rear face sheet debonding during the tests. (c) Shows the effect of changing the rear face sheet attachment condition on the dynamic deflection of the sandwich panels.

Figure 16. (a) The simulated dimensionless maximum dynamic deflections of solid plates and sandwich panels versus the dimensionless impulse applied to the reference solid plates and (b) the permanent panel deflections. Simulations were performed using a fixed standoff distance, H_b = 47.54 cm, to the back face of all the samples.

Figure A.1. Kolsky bar data for the glass microsphere particle tests. The waveforms in (a) and (b) show the pressure measured at the strain gage location for Shots 1 and 3. Figures (c) and (d) show the impulse for test Shots 1 and 3. The four regions of impulsive loading applied to the Kolsky bar are indicated in (c).

Figure A.2. Kolsky bar data for the zirconia particle tests. The waveforms in (a) and (b) show the pressure measured at the strain gage location for Shots 4 and 5. Figures (c) and (d) show the impulse for test Shots 4 and 5. The four regions of impulsive loading applied to the Kolsky bar are indicated in (c).

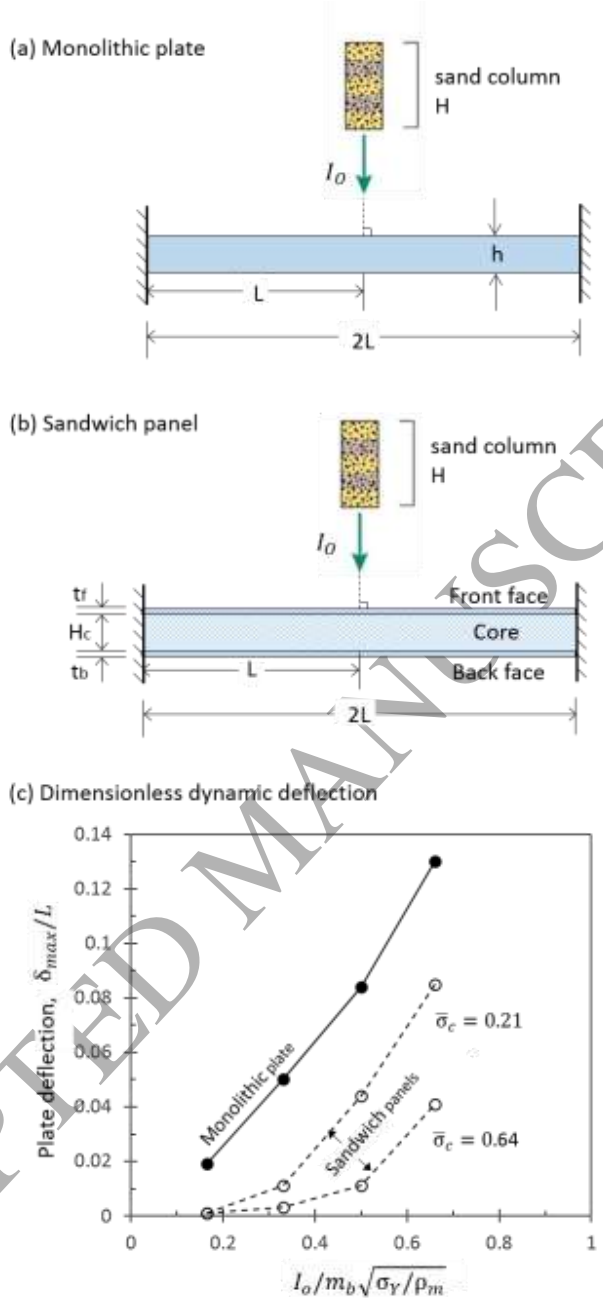

Figure 1 (a) Edge clamped monolithic plate and (b) sandwich panel impacted by a sand slug at normal incidence. (c) Discrete particle predictions of the dimensionless maximum (elastic plus plastic) dynamic deflection of the monolithic plate and two sandwich panels with differing normalized core strengths ($\bar{\sigma}_c$) versus dimensionless impulse. (Adapted from Liu et al. [26])

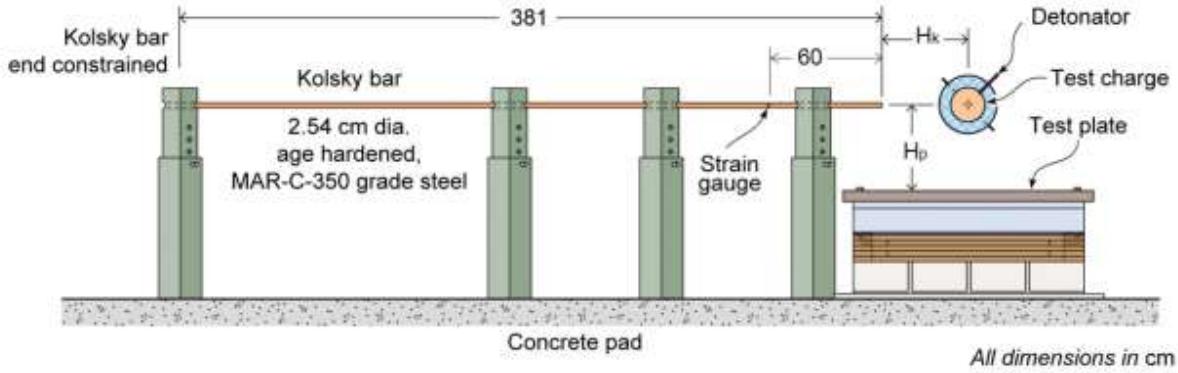

Figure 2 Sandwich panel test setup showing the location of the spherically suspended test charge, the edge restrained sandwich panel, and the strain gage instrumented Kolsky bar used for impulse measurements.

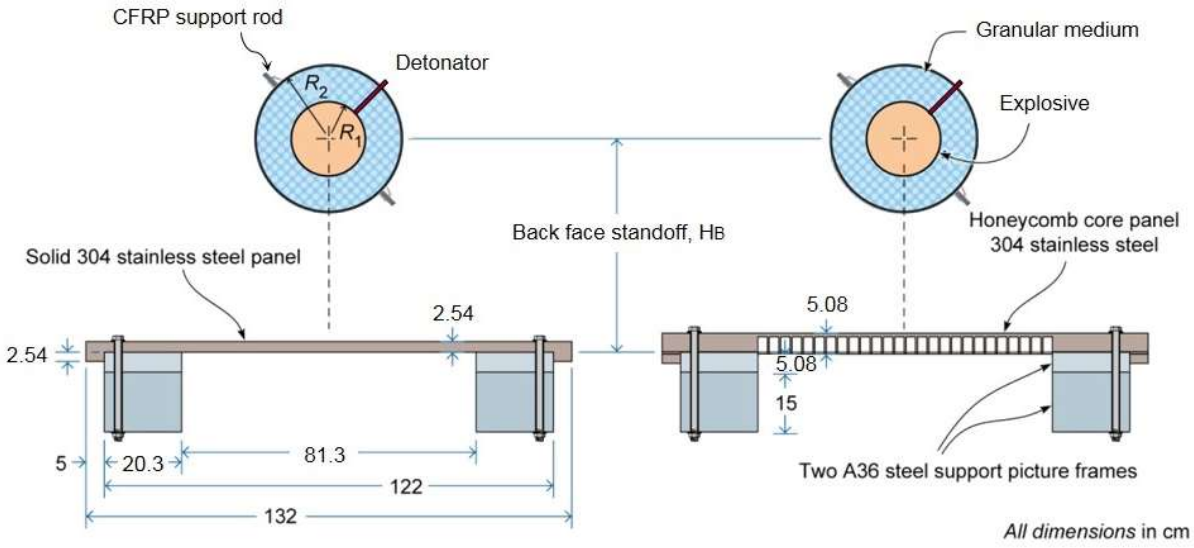

Figure 3 Schematic diagram showing the test arrangement for edge clamped solid plate (left) and equivalent square honeycomb sandwich panel (right). The standoff distance from test charge center to the back face of the solid plate and sandwich panel, H_b, was intended to remain constant for the experimental tests. The standoff distance, H_p, to the target front faces was 2.54 cm smaller for the sandwich due to its greater thickness.

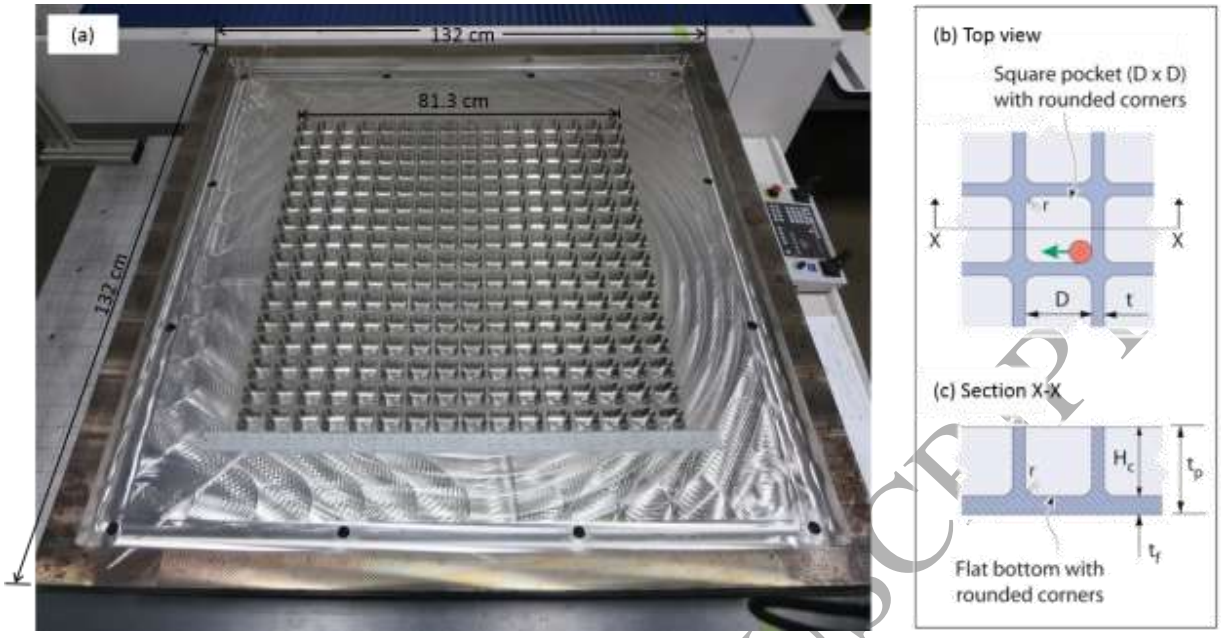

Figure 4 (a) A photograph of the square honeycomb core sandwich panel before the back (bottom) face sheet was attached. The square honeycomb pockets were machined from a thick plate so that the impact side face sheet did not require bonding with the core structure. (b) Shows a schematic view of the cells viewed from above. (c) Shows a schematic illustration of the connection between the front face sheet and the core webs.

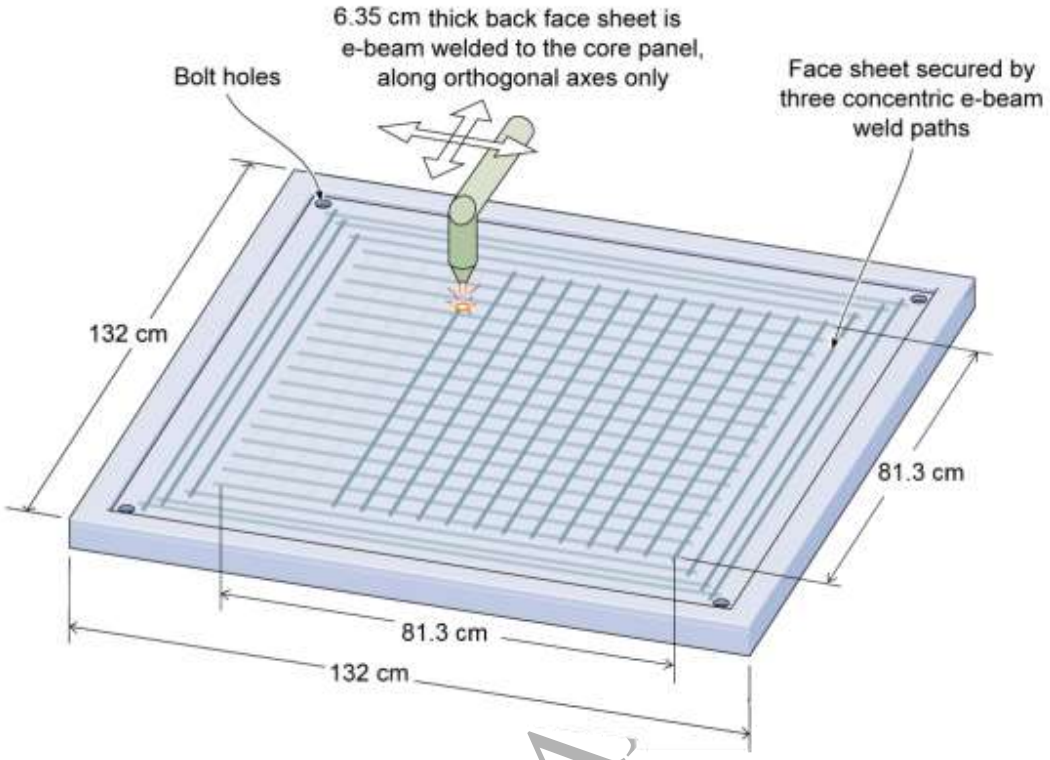

Figure 5 The linear electron beam welding pattern used for attachment of the back face sheet. Each weld line penetrated the back face sheet and center of each honeycomb web to a depth of 3-4 mm. Additional weld lines were used to attach the back face sheet to the 20.3 cm wide solid panel region outside the honeycomb core.

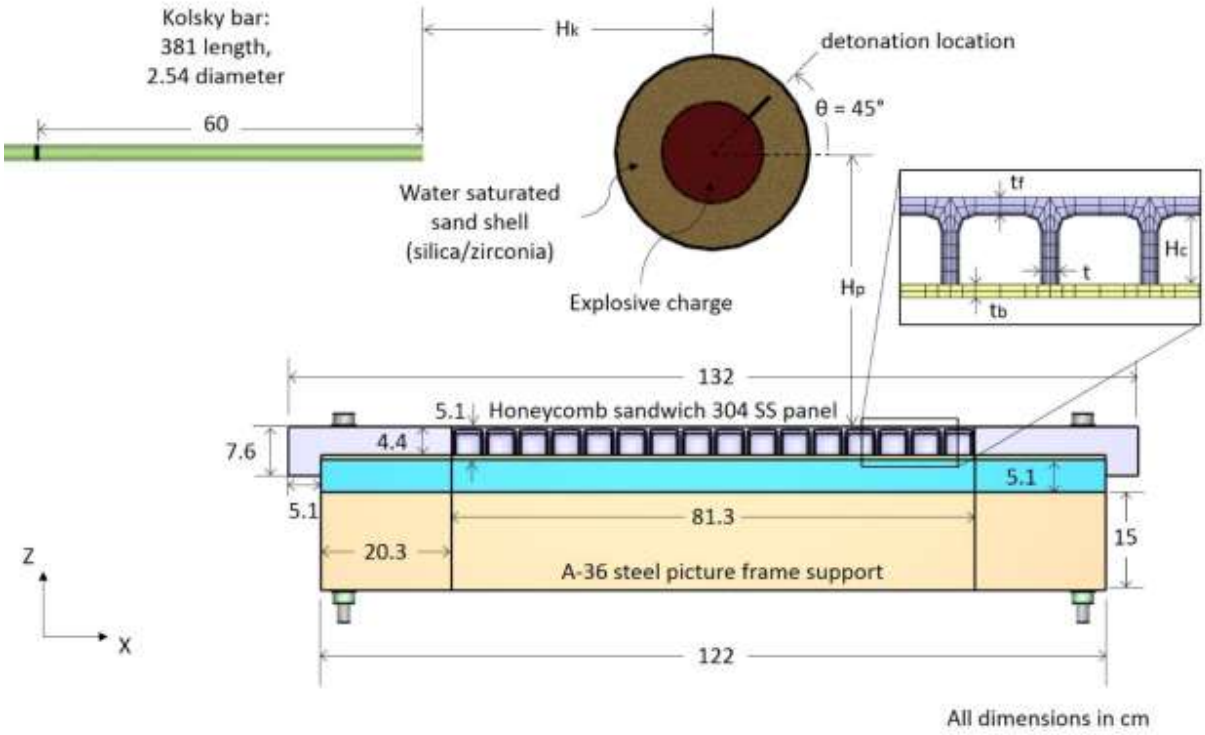

Figure 6 Cross section of the model geometry used for simulations of the tests with an inset showing the mesh used for the honeycomb core and back face sheet.

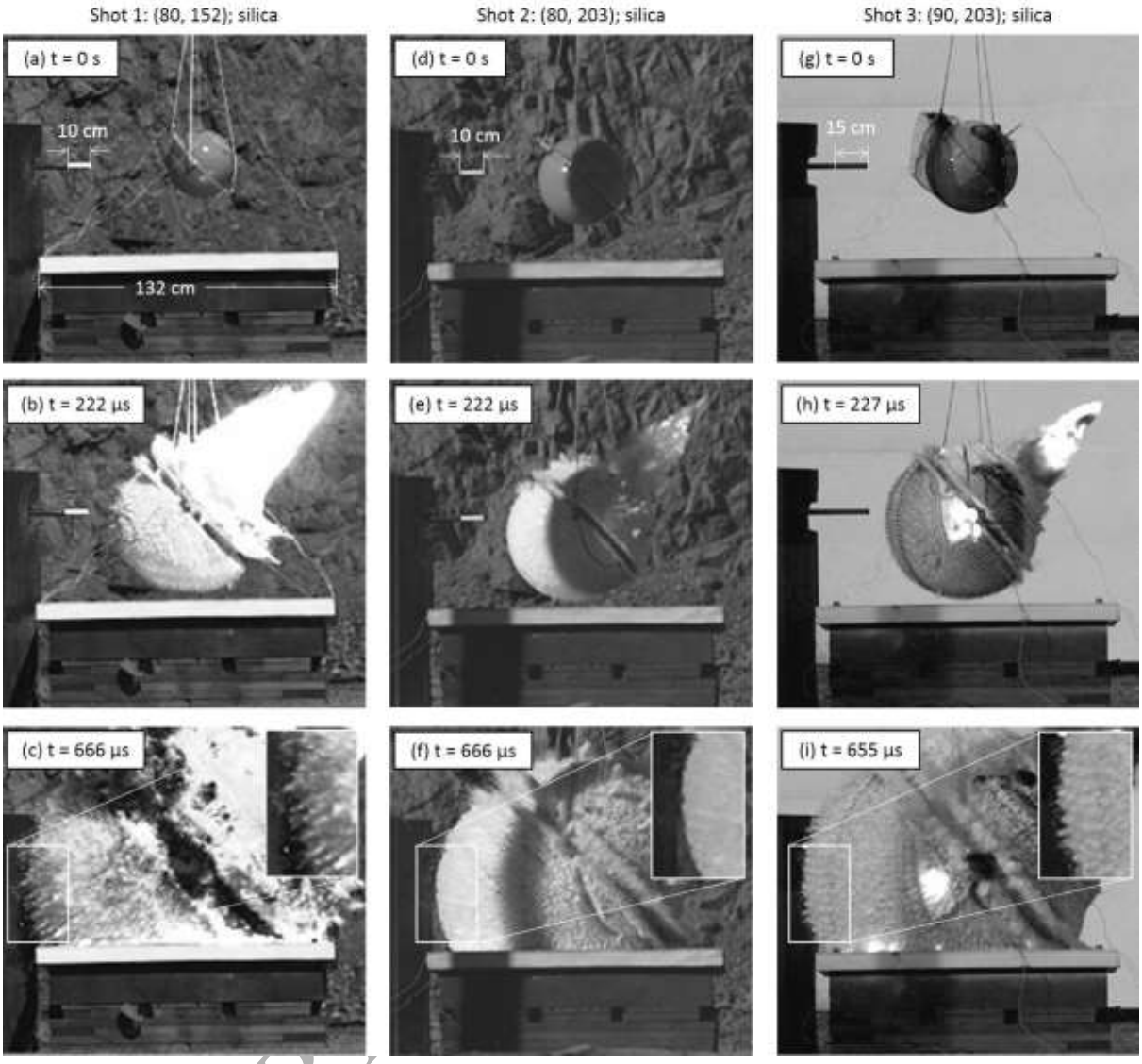

Figure 7 Fused silica microsphere tests with square honeycomb sandwich panels showing approximately equivalent time snapshots for Shot 1 (R1 = 80 mm; R2 = 152 mm; 3 kg explosive charge), Shot 2 (R1 = 80 mm; R2 = 203 mm; 3 kg explosive charge), and Shot 3 (R1 = 90 mm; R2 = 203 mm; 4.5 kg explosive charge).

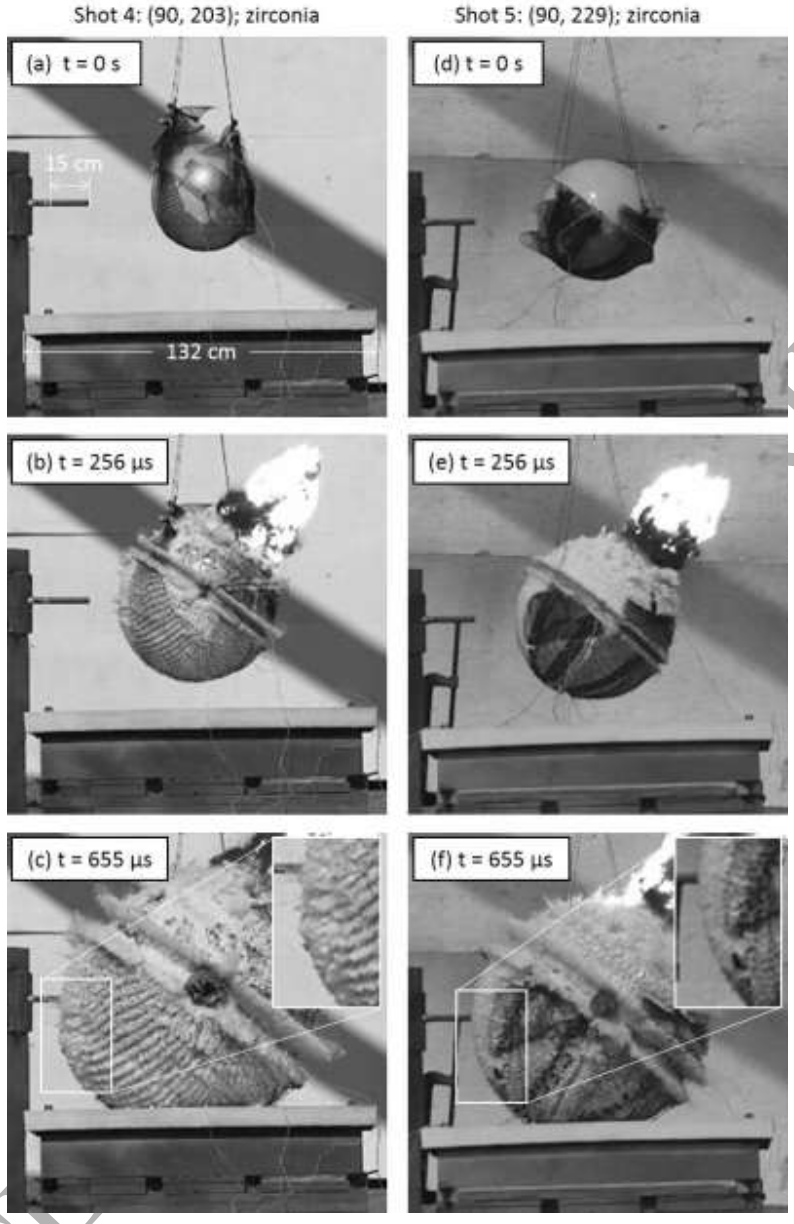

Figure 8 Zirconia particle tests with square honeycomb sandwich panels showing approximately equivalent time snapshots for Shot 4 (R1 = 90 mm; R2 = 203 mm; 4.5 kg explosive charge) and Shot 5 (R1 = 90 mm; R2 = 229 mm; 4.5 kg explosive charge).

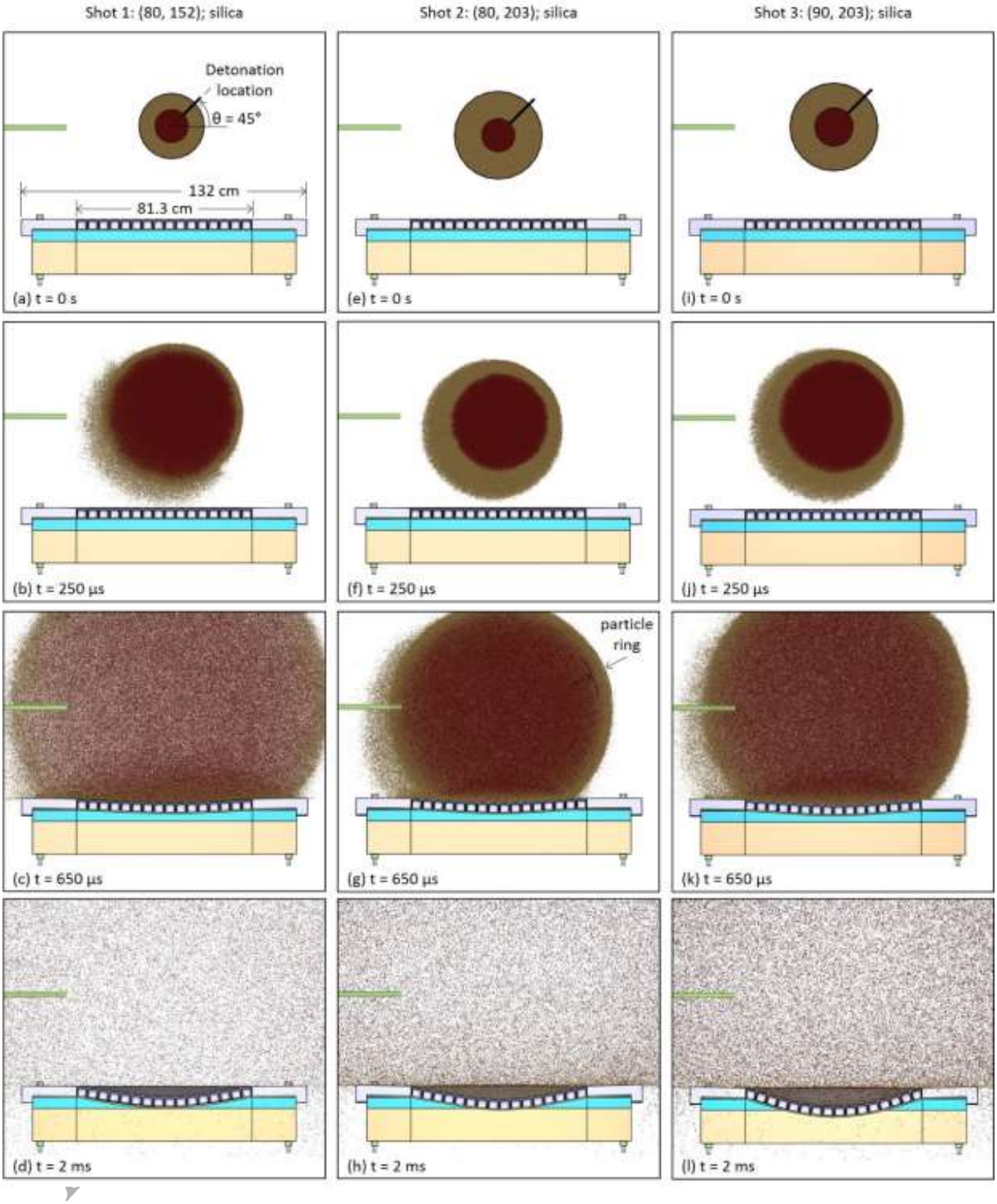

Figure 9 Simulated sand front propagation for the three fused silica particle tests (Shots 1-3) for t = 0 s (the moment of detonation), t = 250 μs, t = 650 μs, and t = 2 ms. The silica particles are tan while the inner red particles are those of the high explosive.

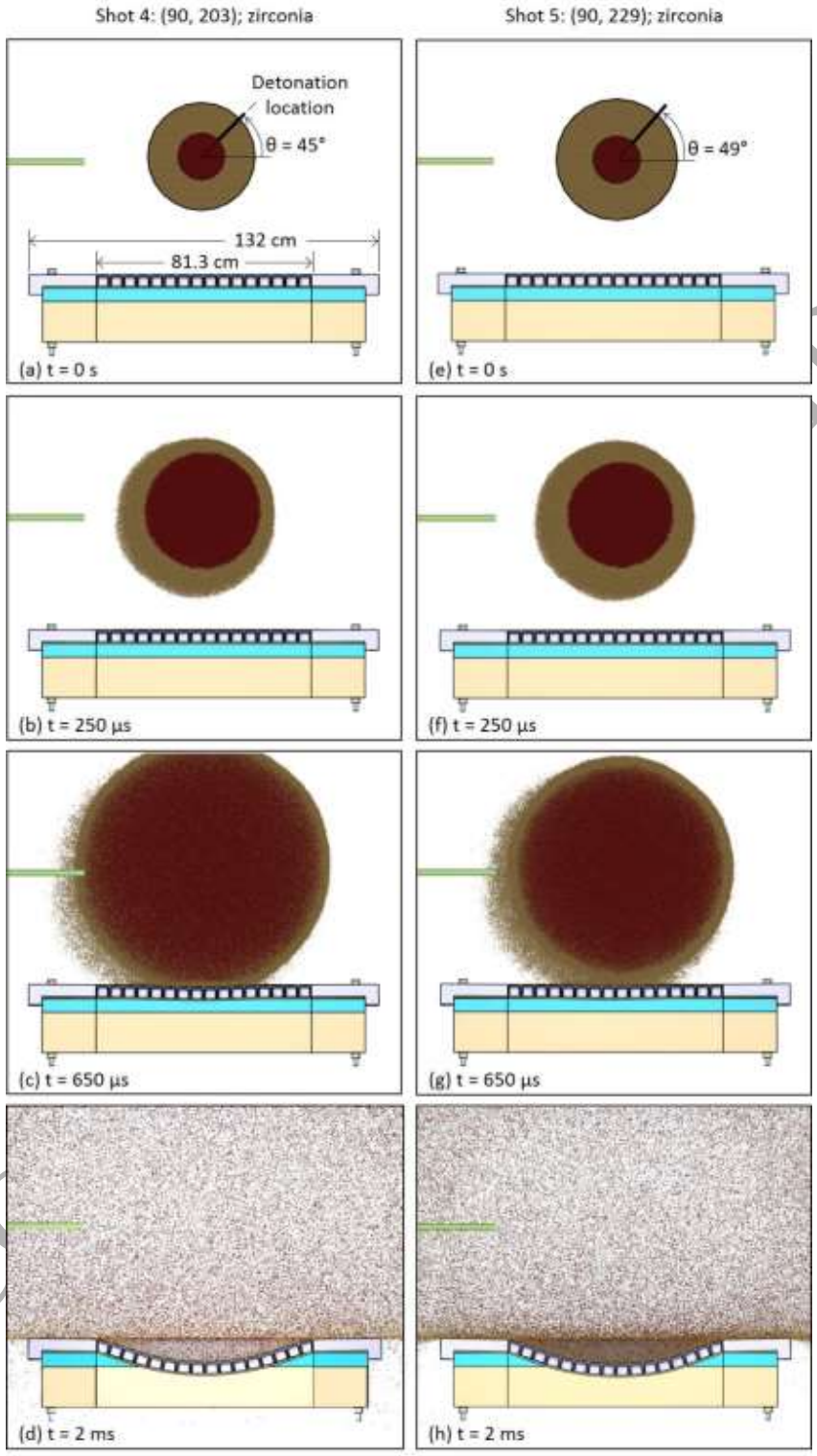
Shot 4: (90, 203); zirconia
Shot 5: (90, 229); zirconia
Detonation location
θ = 45°
132 cm
81.3 cm
θ = 49°
(a) t = 0 s
(e) t = 0 s
(b) t = 250 μs
(f) t = 250 μs
(c) t = 650 μs
(g) t = 650 μs
(d) t = 2 ms
(h) t = 2 ms

Figure 10 Simulated sand front propagation of the two zirconia particle tests (Shots 4 and 5) for t = 0 s (the moment of detonation), t = 250 μs, t = 650 μs, and t = 2 ms. The zirconia particles are tan and the high explosive particles are red.

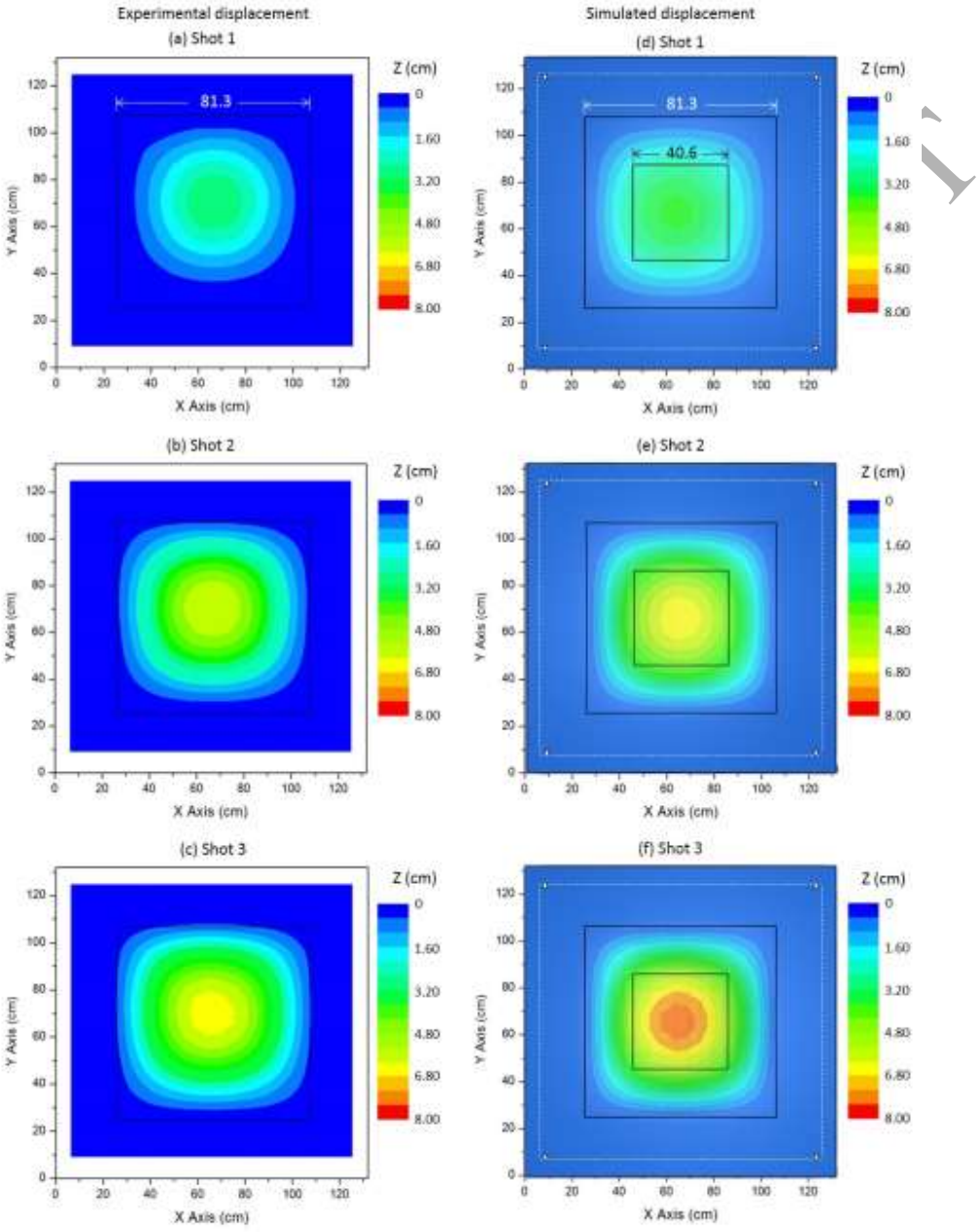

Figure 11 Test panel permanent plastic displacement contour plot in the Z direction for the silica particle tests (Shots 1-3). Experimental profilometry measurements are shown in (a), (b) and (c). These measurements did not include the outer edge (white region) of the panels. The corresponding simulated responses (evaluated at t = 20 ms) are shown in (d), (e), and (f). The 81.3 cm wide black square indicates the edge of the underlying support base and location of the

region with honeycomb cells. The inner, 40.6 cm wide black box indicates the refined mesh region used in the FE model. The 122 mm wide dashed white box in the simulation plots indicates the position of the edge grip from which displacements were determined.

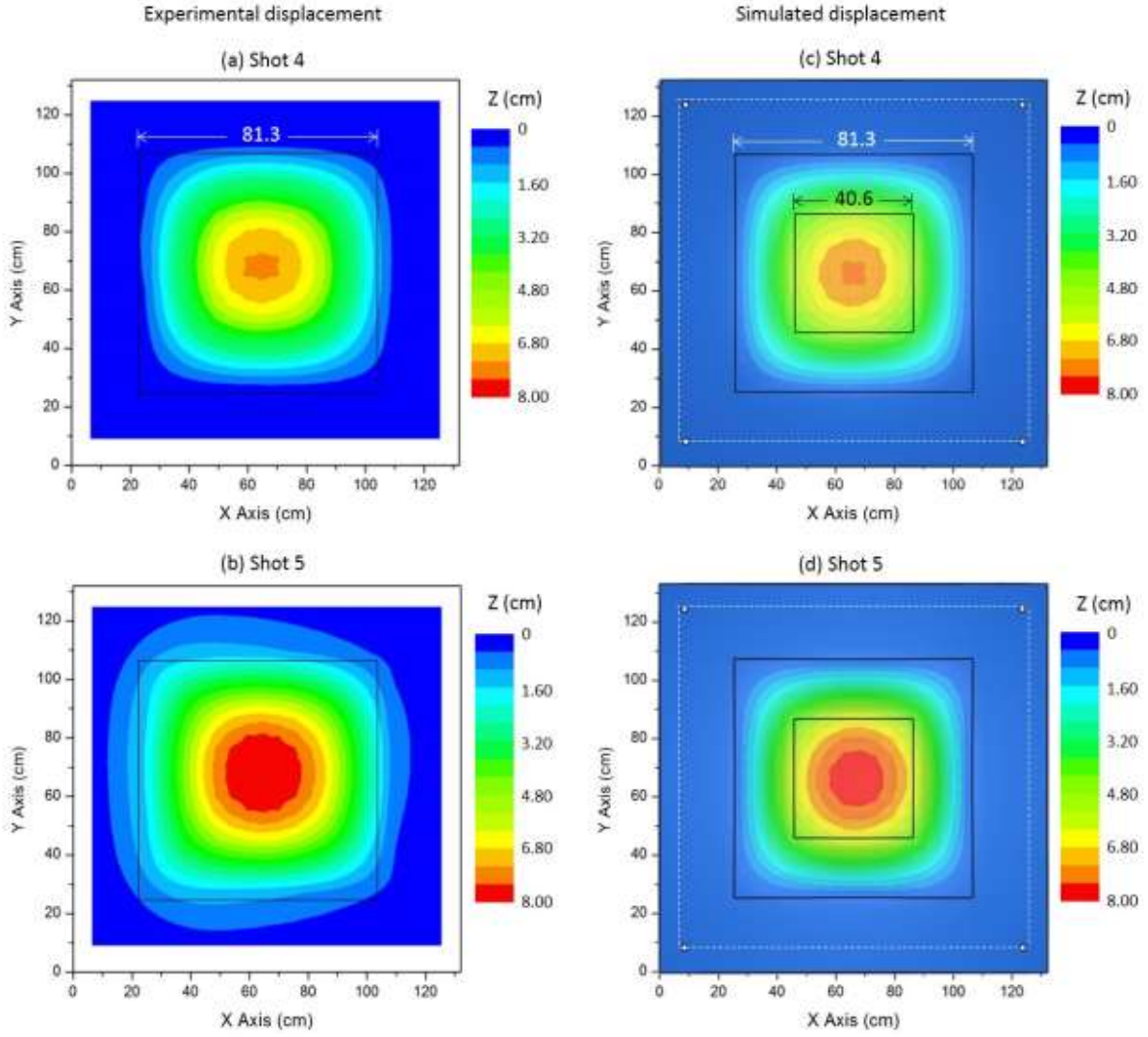

Figure 12 Test panel permanent plastic displacement contour plot in the Z direction for the zirconia particle tests (Shots 4 and 5). Experimental profilometry results are shown in (a) and (b). The simulated responses (at t = 20 ms) are shown in (c) and (d).

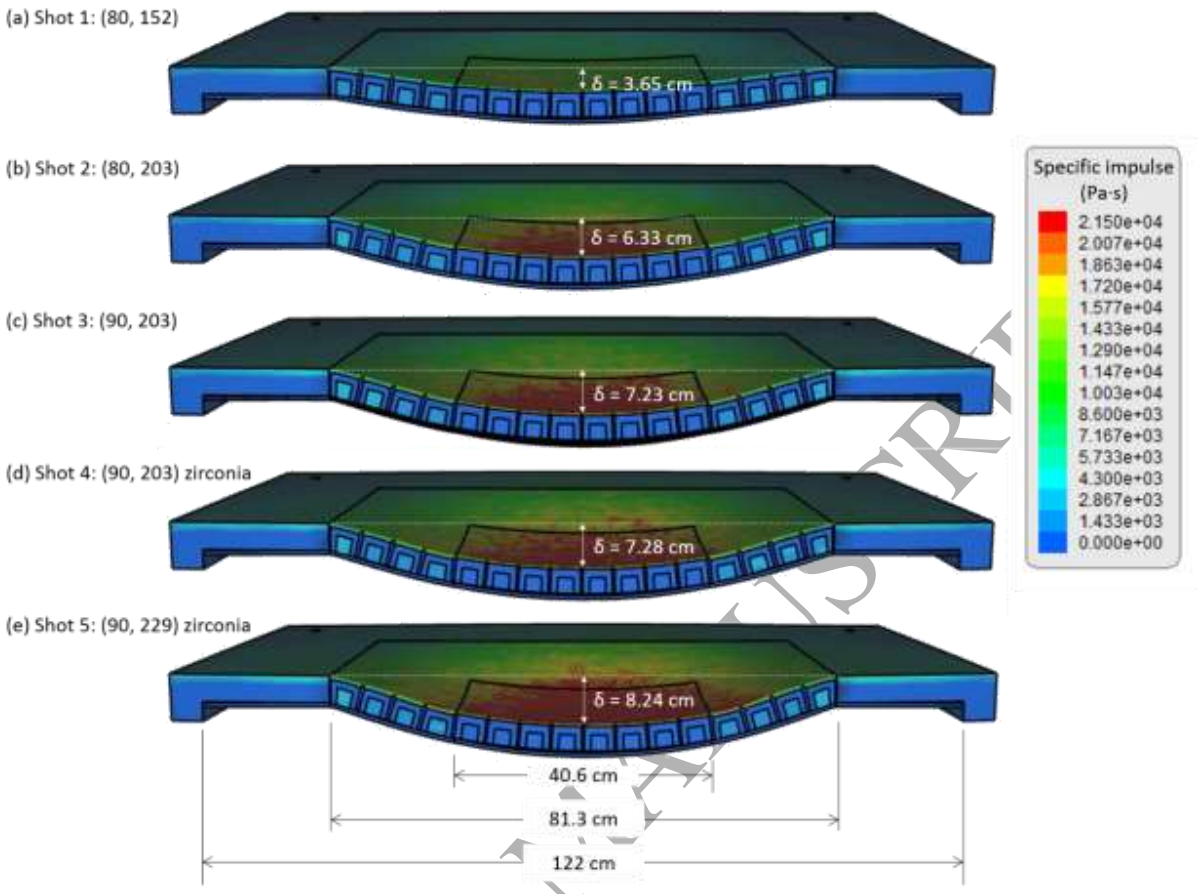

Figure 13 The cross section of the simulated square honeycomb sandwich panels showing the predicted specific impulse distribution applied to the surface by the five test shots. The 81.3 cm wide (unsupported) region of the honeycomb core sandwich section is indicated along with the 40.6 cm wide center region where a refined mesh was used. The predicted permanent deformation and permanent out of plane deflection (δ) is also shown for each test.

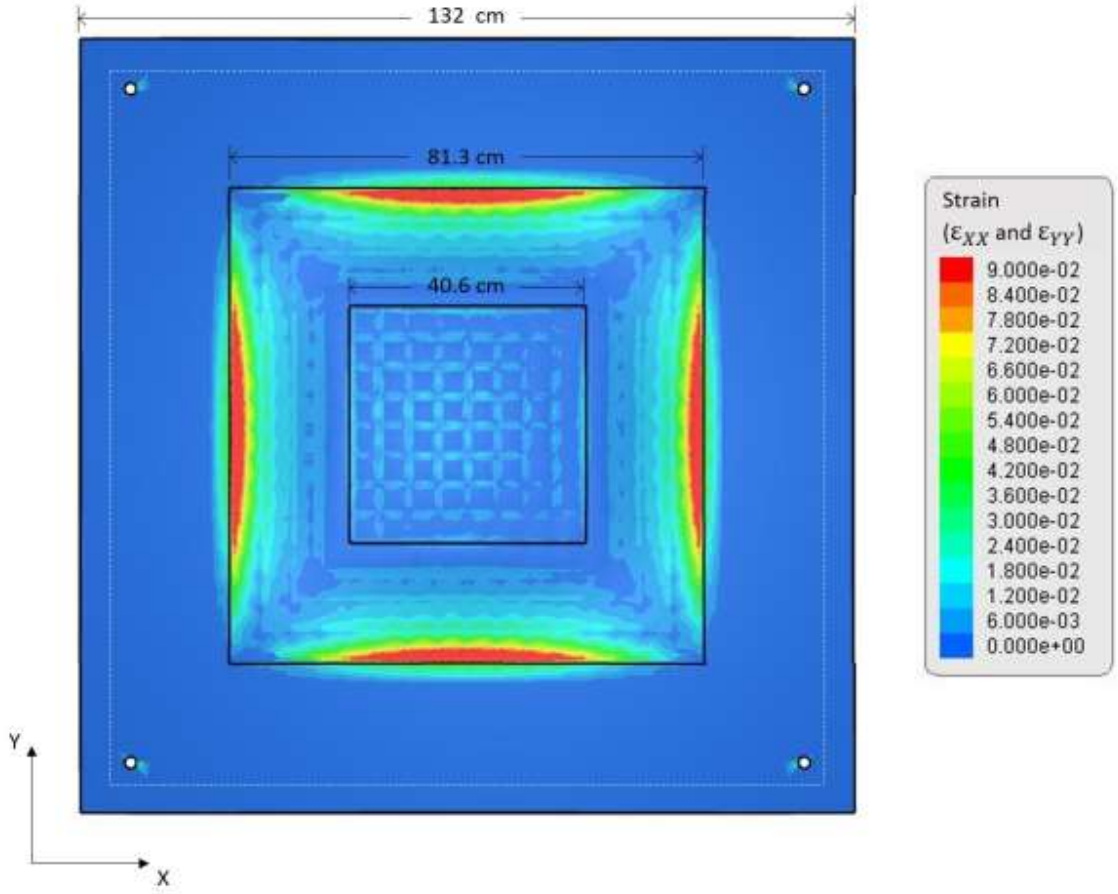

Figure 14 Superposition of the in-plane extensional strains (ε_{XX} and ε_{YY}) on the top face of the honeycomb sandwich panel for Shot 3 after an elapsed time t = 20 ms. The dotted white box indicates the location of the 122 cm wide edge grip.

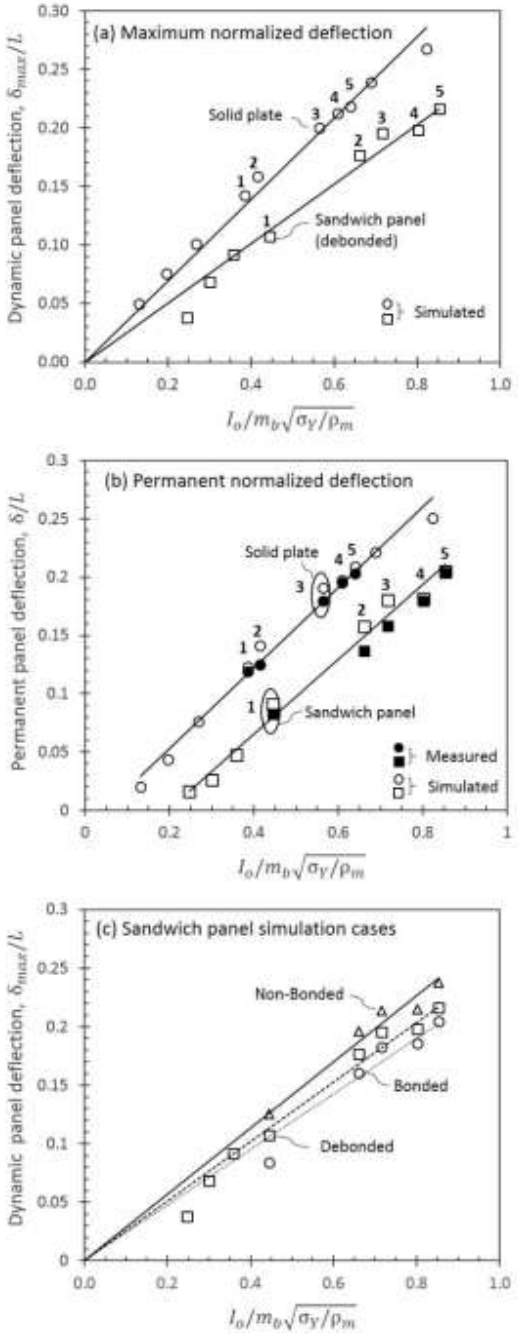

Figure 15 (a) The simulated peak dynamic displacement at the center of the sandwich panels and reference solid plates versus the applied impulse. The numbers adjacent to some data points correspond to the test shot number. The simulations permitted rear face sheet debonding during the impulsive loading of the sandwich panel. (b) The measured and simulated permanent front face displacement at the center of the test structures versus the applied impulse. The sandwich panel simulations again allowed rear face sheet debonding during the tests. (c) Shows the effect

of changing the rear face sheet attachment condition on the dynamic deflection of the sandwich panels.

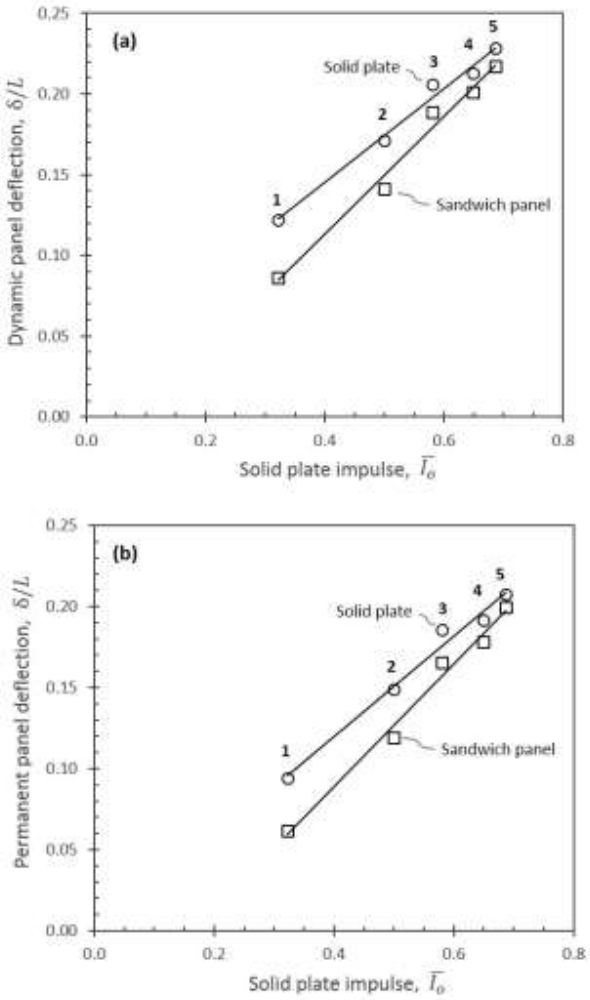

Figure 16 (a) The simulated dimensionless maximum dynamic deflections of solid plates and sandwich panels versus the dimensionless impulse applied to the reference solid plates and (b) the permanent panel deflections. Simulations were performed using a fixed standoff distance, H_b = 47.54 cm, to the back face of all the samples.

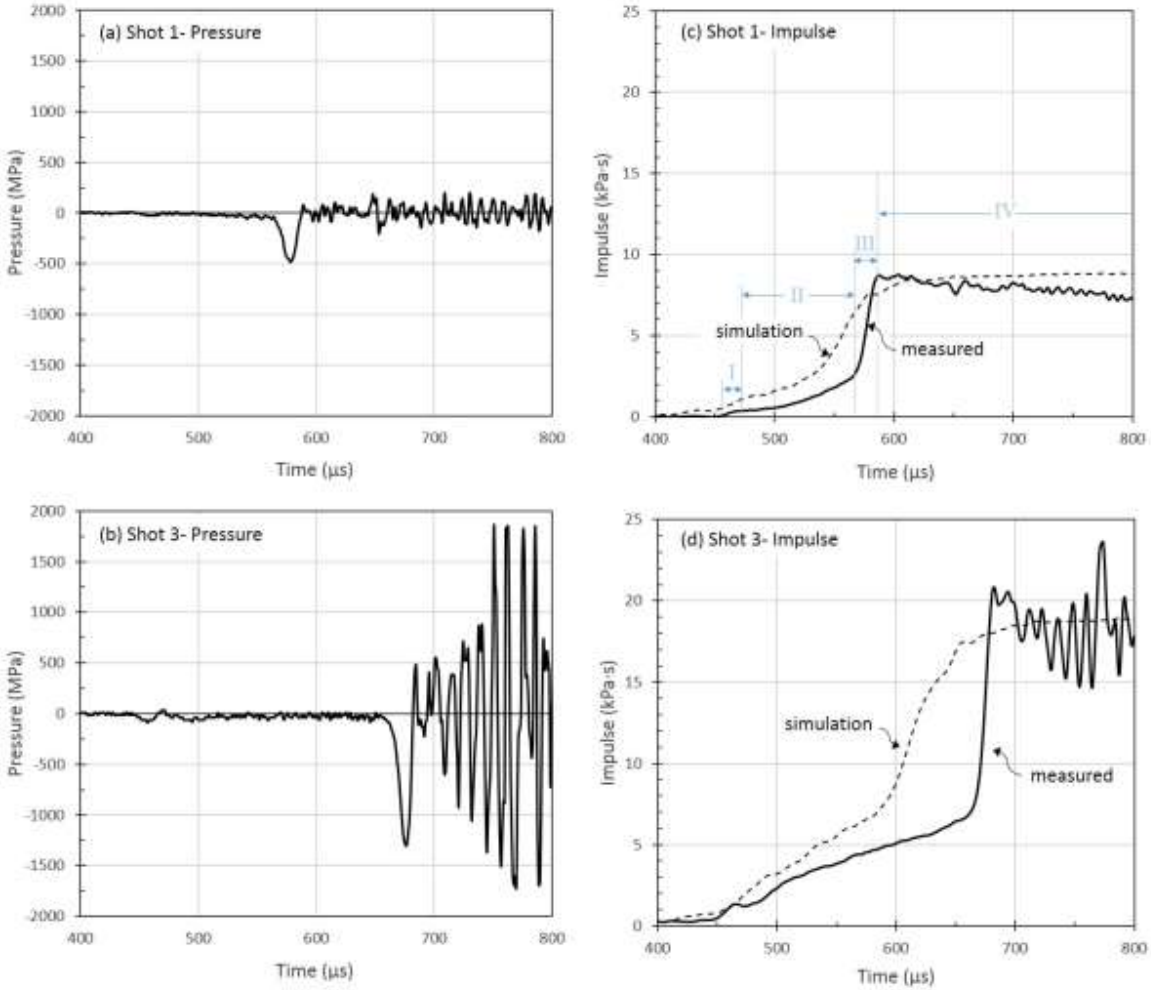

Figure A.1. Kolsky bar data for the glass microsphere particle tests. The waveforms in (a) and (b) show the pressure measured at the strain gage location for Shots 1 and 3. Figures (c) and (d) show the impulse for test Shots 1 and 3. The four regions of impulsive loading applied to the Kolsky bar are indicated in (c).

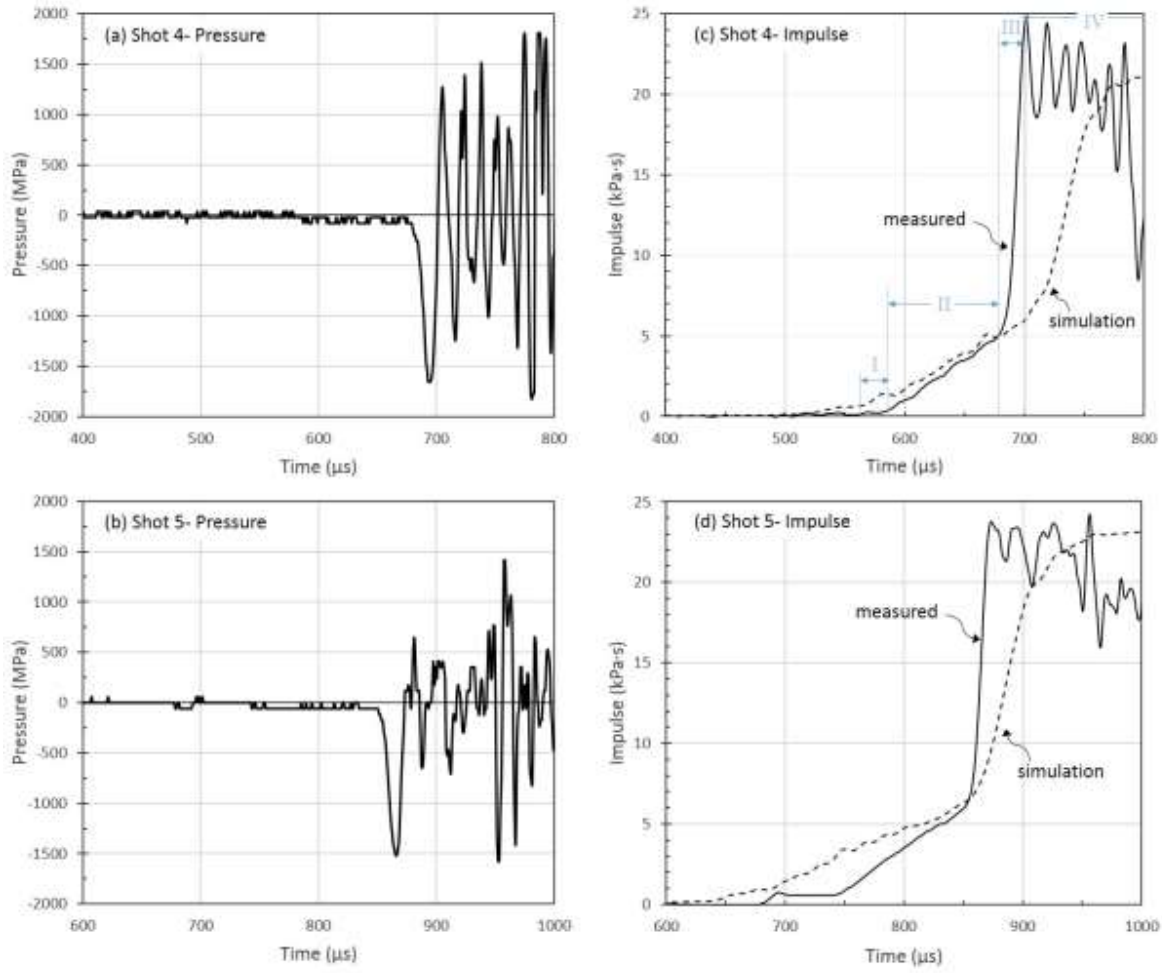

Figure A.2. Kolsky bar data for the zirconia particle tests. The waveforms in (a) and (b) show the pressure measured at the strain gage location for Shots 4 and 5. Figures (c) and (d) show the impulse for test Shots 4 and 5. The four regions of impulsive loading applied to the Kolsky bar are indicated in (c).